Published in final edited form as:
Neuron. 2023 November 15; 111(22): 3604–3618.e11. doi:10.1016/j.neuron.2023.08.002.

BMAL1 loss in oligodendroglia contributes to abnormal myelination and sleep

Daniela Rojo[1], **Louisa Dal Cengio**[1,12], **Anna Badner**[1,12], **Samuel Kim**[1], **Noriaki Sakai**[1], **Jacob Greene**[1], **Tess Dierckx**[1], **Lindsey C. Mehl**[1,2], **Ella Eisinger**[1], **Julia Ransom**[1], **Caroline Arellano-Garcia**[1,3], **Mohammad E. Gumma**[1], **Rebecca L. Soyk**[1], **Cheyanne M. Lewis**[4], **Mable Lam**[5], **Maya K. Weigel**[5,6], **Valentina Martinez Damonte**[1], **Belgin Yalçın**[7], **Samuel E. Jones**[8], **Hanna M. Ollila**[8,9,10,11], **Seiji Nishino**[1], **Erin M. Gibson**[1,13,*]

[1]Department of Psychiatry and Behavioral Sciences, Stanford University School of Medicine; Palo Alto, CA, 94305, USA

[2]Cancer Biology Graduate Program, Stanford University School of Medicine; Palo Alto, CA, 94305, USA

[3]Biology Graduate Program, Stanford University; Palo Alto, CA, 94305, USA

[4]Neuroscience Graduate Program, Stanford University; Palo Alto, CA, 94305, USA

[5]Department of Neurosurgery, Stanford University School of Medicine; Palo Alto, CA, 94305, USA

[6]Stem Cell Biology and Regenerative Medicine Program, Stanford University School of Medicine; Palo Alto, CA, 94305, USA

[7]Department of Neurology & Neurological Sciences, Stanford University School of Medicine; Palo Alto, CA, 94305, USA

[8]Institute for Molecular Medicine, HiLIFE, University of Helsinki; Helsinki, 00014, Finland

[9]Broad Institute of MIT and Harvard; Cambridge, MA, 02142, USA

[10]Center for Genomic Medicine, Massachusetts General Hospital; Boston, MA, 02114, USA

[11]Anesthesia, Critical Care, and Pain Medicine, Massachusetts General Hospital and Harvard Medical School; Boston, MA, 02114, USA

[12]These authors contributed equally

[13]Lead Contact

---

[*] Corresponding: egibson1@stanford.edu.

Authors Contributions:
Conceptualization: EMG, DR, AB, LDC. Methodology: EMG, DR, AB, LDC, SK, TD, JG, EE, CAG, LCM, BY, SEJ, NS, HMO, SN. Investigation: EMG, DR, AB, LDC, SK, TD, JG, EE, CAG, LCM, MEG, RS, JR, SEJ, NS, ML, VMD. Visualization: EMG, DR, AB, SK, JG, EE. Funding acquisition: EMG. Writing: EMG, DR. These authors contributed equally: Anna Badner, Louisa dal Cengio.

Declaration of interests:

Authors declare that they have no competing interests.

Summary:

Myelination depends on maintenance of oligodendrocytes that arise from oligodendrocyte precursor cells (OPCs). We show that OPC-specific proliferation, morphology, and BMAL1 are time-of-day dependent. Knock out of *Bmal1* in mouse OPCs during development disrupts expression of genes associated with circadian rhythms, proliferation, density, morphology, and migration, leading to changes in OPC dynamics in a spatio-temporal manner. Furthermore, these deficits translate into thinner myelin, dysregulated cognitive and motor function, and increased sleep fragmentation. OPC-specific *Bmal1* loss in adulthood does not alter OPC density at baseline but impairs remyelination of a demyelinated lesion driven by changes in OPC morphology and migration. Lastly, we show sleep fragmentation is associated with increased prevalence of the demyelinating disorder multiple sclerosis (MS), suggesting a link between MS and sleep that requires further investigation. These findings have broad mechanistic and therapeutic implications for brain disorders that include both myelin and sleep phenotypes.

Graphical Abstract

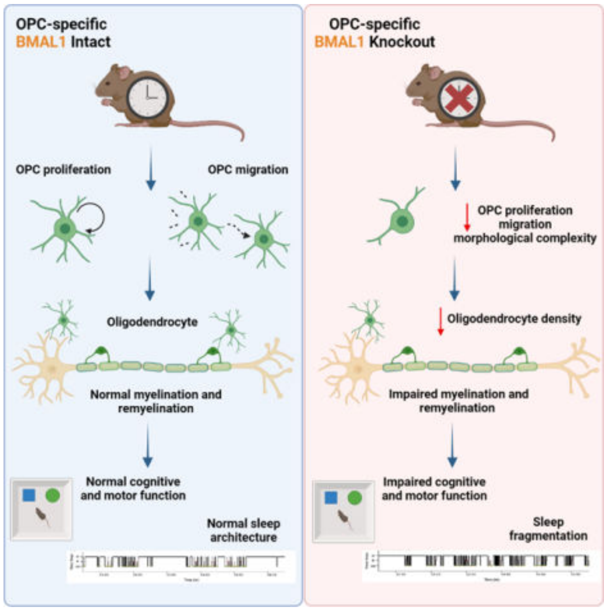

Rojo et al. identified that the circadian transcription factor BMAL1 is necessary to maintain oligodendrocyte precursor cells (OPCs) dynamics in the mouse brain, including proliferation, morphology and migration. Eliminating BMAL1 function specifically in OPCs leads to deficits in myelination and remyelination and abnormal cognitive and motor function and sleep architecture.

Keywords

myelin; OPC; oligodendrocyte; multiple sclerosis; demyelination; BMAL1; sleep; circadian

Introduction

Myelin ensheathes axons to facilitate efficient transduction of electrical signals and metabolic support of neurons.[1,2] Myelin-forming oligodendrocytes arise from oligodendrocyte precursor cells (OPCs), which are evenly distributed throughout the entire central nervous system (CNS). While these cells are remarkably stable in their distribution at the population level, individual OPCs are highly dynamic as the most mitotic cells in the CNS[3,4] with elaborate morphology that promotes motile filopodia and migration. OPC proliferation is stimulated when oligodendroglial loss initiates adjacent OPCs to divide,[5] in response to neuronal activity in some neural circuits,[6] and through biophysical and spatial constraints of their microenvironment.[7] Even though OPCs are a functionally, spatially, and temporally heterogenous precursor population,[8–10] they have a remarkable ability to maintain this consistent homeostatic density in both highly- and lowly-myelinated brain regions, implicating that the function of these cells for circuit optimization may expand beyond myelin production. This unique harmony between prolific cellular self-renewal and population level homeostasis is disrupted in myelin-associated degenerative disorders like multiple sclerosis (MS).[11,12]

From cyanobacteria to humans, temporally dynamic mechanisms are imperative to the maintenance of homeostatic states and behaviors. This is afforded to organisms through the evolution of the circadian system which allows for biological processes to occur at the proper time of day. At the cellular level, circadian rhythms are generated ubiquitously throughout the body by a molecular transcriptional/translational feedback loop that has a period of ~24 hours. Briefly, the products of the core clock genes—*Clock* and *Bmal1* —heterodimerize and drive the transcription of the clock gene families *Period* (*Per*) and *Cryptochrome* (*Cry*). Accumulated levels of PER and CRY within the cytoplasm feed back into the nucleus, displacing the CLOCK and BMAL1 heterodimer and consequently disrupting their own transcription.[13] This transcriptional machinery regulates cytoskeletal factors[14] and cell cycle[15] in numerous cell populations and is required for proper sleep physiology.[16] OPCs proliferate on a circadian cycle[4] and sleep deprivation negatively impacts OPC proliferation and differentiation.[17] The potential role this clock plays in regulating the homeodynamic nature of oligodendroglial lineage cells and if these cells may then contribute to sleep physiology remains to be fully determined.

Numerous lines of evidence support that altered circadian biology is significantly associated with the prevalence of the demyelinating disorder MS, including genetic variability in clock genes such as *BMAL1*,[18] and sleep abnormalities affect the majority of individuals with MS.[19,20] Global disruption of *Bmal1* in mice results in complete abolishment of circadian rhythms and altered sleep architecture in the form of increased total sleep and non-rapid eye movement (NREM), and decreased ability to recover from sleep deprivation.[16] Interestingly, sleep amount but not sleep timing can be rescued by restoring BMAL1 in skeletal muscle,[21] suggesting tissuespecific circadian control can contribute to different components of sleep architecture. We aim to further stratify the regulatory role of BMAL1 in non-neuronal populations by investigating how this transcription factor regulates the homeodynamic nature of oligodendroglial lineage cells and myelination and the putative contributions to maintenance of circuit-level neurological processes.

Results

Time of day-dependent changes in OPC dynamics

Previous work has suggested that OPC proliferation and differentiation is time-of-day dependent.[4,17] To determine if this is regionally specific and whether there also exist differences in OPC dynamics in a time-of-day-dependent manner in mice, we assessed OPC proliferation and morphology in both grey matter and white matter at zeitgeber time (ZT) 0 (lights on) and ZT12 (lights off) using a single pulse of the thymidine analogue 5-ethynyl-2’-deoxyuridine (EdU) to mark newly proliferating OPCs. OPC population densities did not differ between ZT0 and ZT12 in both the cortex and corpus callosum; however, in the cortex, OPC proliferation was significantly reduced at ZT12 compared to ZT0 (Figure 1A), and OPC filament volume was significantly increased at ZT12 (Figure 1B–C). These data suggest that OPC function may be regulated in a circadian manner. To investigate this, we first examined expression of the molecular clock machinery throughout the oligodendroglial lineage using the mouse brain transcriptome database of cell type-specific gene expression[22] and directly confirmed BMAL1 expression in mouse OPCs (Figure S1A–B). We analyzed BMAL1 expression in OPCs at ZT0 and ZT12 and identified an increase in OPC-specific BMAL1 intensity at ZT12 compared to ZT0 in both the cortex and corpus callosum (Figure 1D). We then isolated OPCs from postnatal day 6 (P6) mice that express a fusion protein of PER2 and LUCIFERASE and confirmed BMAL1 expression in cultured OPCs (Figure 1E). OPCs show 24-hr oscillations of rhythmic clock gene expression *in vitro* assessed by measuring luminescence for 48-hrs following synchronization with two commonly used synchronizing agents *in vitro*, dexamethasone (Figure 1F) or forskolin (Figure S1C). Altogether, these results show that OPCs express a functional circadian clock and are subject to time-of-day changes in OPC dynamics.

Functional loss of Bmal1 during embryonic development dysregulates OPC proliferation and morphology in a region-specific manner

We next developed a model to specifically knock out the *Bmal1* DNA-binding domain in OPCs during embryonic development by crossing clock gene knock out (*Bmal1*$^{fl/fl}$*)* and cell type-specific Cre driver *(NG2::Cre*) mice to generate a *Bmal1* transcriptional hypomorph that significantly decreased BMAL1 levels specifically in OPCs (*NG2:Cre+;Bmal1*$^{fl/fl}$ or OPC-*Bmal1*-KO) (Figure 1G; Figure S1D–E). The *Bmal1*^{flox} mouse line is a commonly used line in circadian research to investigate cell-specific deletion of the molecular circadian clock.[23] Importantly, knock out of this functional BMAL1 binding domain in OPCs dysregulated 24-hr rhythms of OPC clock genes (*Bmal1*, *Per2*, and *Rev-Erbα*) following synchronization *in vitro* (Figure 1H).

To understand how *Bmal1* in OPCs may contribute to establishment and maintenance of the OPC population, we first discerned the role this transcription factor plays in homeostatic maintenance of OPCs throughout the brain, including various brain regions implicated in motor, cognitive, and sleep control (Figure 2A), such as cortex,[24] corpus callosum,[25–28] hypothalamus,[29] and brainstem.[30] OPC-*Bmal1*-KO and WT mice were injected with EdU on P18–20 to mark newly proliferated OPCs. EdU^{+}/PDGFRα^{+} OPCs were significantly reduced in the corpus callosum of P21 OPC-*Bmal1*-KO compared to WT mice without resultant volume changes of the white matter tract (Figure 2B–C; Figure S1F), but not in other brain regions, such as the cortex, the medial and lateral preoptic area (MPOA; LPOA), the dorsomedial and lateral hypothalamus (DMH; LH), the locus coeruleus, and pontine nucleus (Figure 2C; Figure S2A). *Bmal1* loss significantly reduced OPC density in the corpus callosum, cortex and locus coeruleus (Figure 2D–E), but not in other brain regions (Figure S2B), that persisted into adulthood (P63; 5527 ± 221.7 vs 4289 ± 355 cells/mm3; $n = 4–6$ mice; $P < 0.05$). Similarly, *Bmal1* loss significantly decreased OPC morphological complexity in the corpus callosum, cortex and locus coeruleus (Figure 2F–G). Thus, BMAL1 regulates OPC proliferation, density, and morphological complexity in a region-specific manner.

BMAL1 regulates OPC density establishment during embryonic development through defects in migration

Our finding that BMAL1 regulates OPC population maintenance in select brain regions suggests a spatio-temporal importance in the proper establishment of oligodendroglial lineage cells during early-life brain development. Given that density differences in the cortex and locus coeruleus are not accounted for by changes in OPC proliferation (Figure 2), we hypothesized that the loss of *Bmal1* in OPCs may impact their ability to migrate from the germinal areas to colonize regions of the forebrain based on the significant changes in morphological complexity. To test this, we evaluated the developing mouse brain at P0, after completion of the major waves of OPC migration from the germinal areas towards the cortex and tuberal hypothalamus.[31] We analyzed the number of OPCs in the areas adjacent to the germinal subventricular (Figure 2H–I) and third ventricular zone (Figure S2D–G). We found that even though the absolute OPC density did not change in the germinal areas (Figure 2J, Figure S2F), the OPC density across the developing cortex and lateral hypothalamus was significantly reduced in OPC-*Bmal1*-KO mice due to a reduction in the number of migrating OPCs away from the germinal areas (Figure 2K, Figure S2G). Moreover, when we evaluated isolated OPCs from P6 OPC-*Bmal1*-KO mice in the presence of anti-mitotic agents to control for proliferation differences between genotypes, the dysregulation of *Bmal1* in OPCs led to significant deficits in migration *in vitro* (Figure 2L–N), consistent with the deficits in OPC establishment found *in vivo*.

BMAL1 controls the expression of genes that contribute to OPC homeostasis

It is possible that the effects observed in the OPC-*Bmal1*-KO are due to a variety of downstream pathways controlled by BMAL1. To test the role of BMAL1 as a transcriptional regulator in OPCs, we isolated OPCs from P6–7 OPC-*Bmal1*-WT and OPC-*Bmal1*-KO mice at 6-hr intervals for 24 hrs. We then performed RNA sequencing followed by circadian rhythmicity assessment of the transcriptomes using JTK-Cycle analysis[32] (Figure 3A–D, Figure S3A–B). We found that approximately 10% of genes are rhythmically expressed in OPCs (Figure 3A–D, Table S1), with an enrichment in rhythmic genes that code for modulators of mitosis, apoptosis, and transcriptional function (Figure S3C). To assess time-of-day expression changes in circadian intact OPCs, we evaluated differential expressed genes (DEGs) in OPCs from OPC-*Bmal1*-WT mice at ZT0 compared to ZT12, the time points of *Bmal1* trough and peak expression, respectively (Figure 1D, H). The gene ontology analysis revealed that pathways related to regulation of cell cycle, apoptosis, oligodendrocyte differentiation, gliogenesis, and microtubule binding have a time-dependent variation in OPCs (Figure 3A). These include a downregulation at ZT0 of cell cycle and migration regulators like *Egr4*, *Cebpb*, *Atf3* and *Atf4*, *Dusp2* and *Dusp5*, *Pim1* and *Pim3*, and *Btg1* and factors that determine oligodendrocyte lineage specification like *Id2* and *Tnf* (Figure 3B–C, Table S2). Around half of the oscillating genes in OPCs (1496 out of 2794 genes), particularly related to mitosis control, lose rhythmicity in OPCs lacking functional *Bmal1* (Figure 3D right, Figure S3D). Loss of BMAL1 decreased the expression at ZT12 of genes linked with cytoskeletal regulation and migration (*Tubb6*, *Mark4*, *Sirt2*, *Cdk5*, *Crocc*, *Pim1*, *Pim3, Smad7, Tgfb1, Bmp4, Bmp7*), cell cycle (*Egr3*, *Egr4*, *Cdkn1a*, *Klf4*, *Plk3*, *Btg2*), OPC proliferation (*Cspg4*, *Wnt4*, *Id2*, *Sox2*), and OPC differentiation (*Sox10*, *Olig1*, *Olig2*, *Myrf*, *Sirt2*, *Cdk5*) (Figure 3E–H, Table S3). The Reactome Enrichment Analysis indicates that the mitotic cell cycle pathway is the most disrupted in OPCs lacking functional BMAL1 at ZT12 (138 genes, p adj = 0.0132; Figure S3E–F). We also found a downregulation in OPCs lacking functional *Bmal1* of modulators of synapses (*Neurl1a*, *Clstn1*, *Stx1a*) and inflammation (*Smad7*, *Bmp4*, *Bmp7*, *Tnf*, *Tgfb1*, *Ccl4*, *Atf3*, *Atf4*, *Cebpb*), supporting a role for BMAL1 in non-myelinating functions of OPCs (Figure 3E–H, Figure S3E–F). The decrease in *Sirt2*, *Cdk5, Bmp4/7 and Tnfb1* expression in OPCs following BMAL1 loss further suggests that BMAL1 contributes to the regulation of cytoskeletal factors, complexity, and migration in OPCs, factors known to play a vital role in their ability to maintain equal distribution throughout the brain parenchyma.[5,33–35] Interestingly, we also found that the expression of *Htt* and *Snx33* genes increases in OPCs lacking *Bmal1*. Both genes have been previously associated with neurodegenerative disorders[36–38] and their aberrant expression is linked to deficits in axonal myelination[39] and amyloid precursor protein trafficking.[40] Altogether, these results indicate that BMAL1 acts as a transcriptional regulator of OPCs by controlling genes that are critical for OPC dynamics.

OPC-specific Bmal1 knock out dysregulates oligodendrocytes and myelination

Because a decrease in OPC density impacts the progenitor pool available for oligodendrogenesis, and considering we identified a downregulation of genes that control OPC differentiation, we then evaluated the effect of OPC-specific *Bmal1* loss throughout the oligodendroglial lineage. OPC-*Bmal1*-KO mice exhibited a significant decrease in CC1$^+$ oligodendrocyte density in the corpus callosum, cortex and locus coeruleus (Figure 4A–B), and MPOA (Figure S2C) at P21, an age that corresponds to the end of developmental myelination. We next investigated if the cellular effects of *Bmal1* loss in OPCs were a consequence of decreased OPC number exclusively or potentiated by dysregulated differentiation potential. In OPCs isolated from P6 OPC-*Bmal1*-KO or WT mice, we found a 14% decrease in proliferating EdU$^+$/PDGFRα^+ cells in *Bmal1* knock out compared to control OPCs (Figure S4A–B). We then induced OPC differentiation for 3 days and found a significant decrease in MBP$^+$ oligodendrocytes when *Bmal1* was knocked out (Figure S4C–D) that recovered when differentiation was completed after 6 days in both genotypes (Figure S4E–F).

We next assessed how these cellular changes impacted myelination in the corpus callosum, a white matter tract that contributes to a diverse range of neurological functions from cognitive and motor[6,41] to sleep.[25–28] Using transmission electron microscopy (TEM), we observed hypomyelination in the form of thinner myelin sheaths of small and medium caliber axons in the frontal lobe corpus callosum of OPC-*Bmal1*-KO compared to control mice (Figure 4C–F). We did not identify any decrements in axonal health as assessed by measuring intra-axonal organelle accumulation or changes in the frequency distribution of myelinated axon diameters between genotypes (Figure S1G).

As NG2 is a proteoglycan that is expressed in OPCs and pericytes, *Bmal1* loss in NG2$^+$ cells could potentially compromise the blood-brain barrier (BBB), leading to brain inflammation and neurotoxicity inducing oligodendroglia and myelin loss. Brain-wide loss of *Bmal1* has been linked to BBB hyperpermeability associated with platelet-derived growth factor receptor β dysregulation.[42] To rule out this possibility, we tested the integrity of the BBB through administration of sodium fluoresceine and found no differences in brain permeability between genotypes (Figure S1H). We also assessed pericyte coverage of microvasculature using CD13$^+$/CD31$^+$ and found no significant differences between genotypes (Figure S1I).

Loss of Bmal1 in oligodendroglial lineage cells disrupts white-matter associated motor and cognitive function

We next evaluated if these cellular and myelin decrements could contribute to dysregulated circuit function, specifically focusing on established motor and cognitive behaviors known to be affected by hypomyelination within frontal lobe corpus callosum.[6,41,43] The identified oligodendroglial dysregulation in OPC-*Bmal1*-KO mice produced a significant disruption of gait, including a decrease in paw swing speed and stride length (Figure 4G). We also tested white matter-associated cognition using a modified novel object recognition test (NORT) that places greater emphasis on attention and short-term memory instead of hippocampal-dependent long-term memory.[41,43] OPC-*Bmal1*-WT mice spent more time investigating the novel over familiar object while OPC-*Bmal1*-KO mice did not discriminate between the objects during the testing phase, suggesting deficits in white matter-associated cognition (Figure 4H). These data support the finding that BMAL1 functional loss in OPCs and resultant hypomyelination affect white matter-associated circuit function.

BMAL1-driven deficits in oligodendroglia during embryonic development are associated with abnormal sleep in mice

BMAL1 is necessary for proper sleep control and its global disruption in mice completely abolishes circadian rhythms and sleep homeostasis.[16] Given that oligodendroglial lineage cells in the cortex, corpus callosum and locus coeruleus are particularly affected by *Bmal1* loss and that these regions are involved in regulation of sleep, including NREM sleep and sleep to wake transitions,[24,26–28,44,45] we posited that sleep/wake architecture may be dysregulated in mice that lack functional *Bmal1* in OPCs. We subjected OPC-*Bmal1*-KO and OPC-*Bmal1*-WT mice to a 12::12 light/dark (LD) cycle for 7 days to first evaluate circadian entrainment followed by constant darkness (DD) for 15 days to assess free-running circadian rhythms (Figure 5A). OPC-*Bmal1*-KO mice exhibited normal circadian periods in activity (tau) compared to controls with no genotype effect on overall locomotor activity (Figure S5A–C). At 3.5 months old, we implanted electroencephalogram (EEG) electrodes above the cortex of OPC-*Bmal1*-WT and OPC-*Bmal1*-KO mice to measure sleep waves and evaluated baseline sleep recordings in light::dark cycles. In mice, sleep is polyphasic, and around two thirds of these short sleep periods occur during the light/rest phase.[46] Under normal sleep conditions (baseline, BL), the total wake, and thus sleep, time did not vary between genotypes during either light or dark phases (Figure 5B left). However, when we evaluated sleep/wake architecture, OPC-*Bmal1* KO led to significant fragmentation during the dark/active phase; OPC-*Bmal1*-KO mice had 29% shorter but 57% more frequent wake events (Figure 5C–D left, 5H). Sleep is characterized by two main stages consisting of rapid eye movement (REM) and NREM sleep, the latter of which is particularly important for plasticity, recovery, and information processing.[47] During the dark/active phase, NREM sleep events were also fragmented with shorter but more frequent bouts despite no differences in total time spent in NREM sleep at baseline (Figure 5E–G left, 5H). REM sleep did not vary between genotypes (Figure S5D–F).

To further elucidate the effect of oligodendroglial dysregulation in our OPC-specific BMAL1 KO mice on sleep homeostasis, we subjected mice to a 6-hr sleep deprivation challenge. The effect on fragmentation was exacerbated in OPC-*Bmal1*-KO mice following sleep deprivation as the total amount of wake was decreased in the dark/active phase and wake events were 49% shorter and 95% more frequent than controls (Figure 5B–D right). OPC-*Bmal1*-KO mice exhibited increased total time spent in NREM during the dark/active phase compared to OPC-*Bmal1*-WT mice and the events were shorter and more frequent following sleep deprivation (Figure 5E–G right). Taken together, these findings reveal that the homeostatic dysregulation of oligodendroglial lineage cells due to *Bmal1* loss is associated with increased sleep fragmentation and a greater drive for restorative NREM sleep following sleep deprivation. These findings provide a hitherto underappreciated link between oligodendroglial processes and healthy sleep function, a connection that may be relevant to a range of neurological diseases.

Functional loss of Bmal1 in adolescence leads to dysregulated OPC dynamics and sleep fragmentation

As the two major waves of OPC migration that establish OPC density occur during mid-embryonic development[31] and developmental oligodendrogenesis is completed before early adulthood in mice, we hypothesized that *Bmal1* disruption in OPCs later in life would result in less dramatic effects on OPC dynamics and subsequent sleep architecture. To investigate this, we induced knock out of *Bmal1* in OPCs using a conditional, inducible OPC-specific Cre mouse line $PDGFR\alpha::CreER^{T2}$ crossed with $Bmal1^{fl/fl}$ mice. $PDGFR\alpha::CreER^{T2}$+;$Bmal1^{fl/fl}$ (OPC-*Bmal1*-iKO) and $PDGFR\alpha::CreER^{T2}$-;$Bmal1^{fl/fl}$ (OPC-*Bmal1*-WT) mice were injected intraperitoneally with 100 mg/kg tamoxifen for 3 consecutive days starting at P18. Similar to the embryonic OPC knock out,[48] this 3-day tamoxifen schedule leads to 80% recombination,[43] with no evidence of 'leaky' Cre expression in neurons.[49] Knock out of *Bmal1* during adolescence similarly led to significant but more subtle deficits in OPC density and morphological complexity (Figure S6A–E), indicating a consistent change in OPCs following *Bmal1* loss in both OPC-specific Cre mouse lines (*NG2:Cre* and $PDGFR\alpha::CreER^{T2}$). However, these cellular deficits did not translate into changes in myelin sheath thickness (Figure S6F–G).

We next recorded sleep waves at baseline in mice at 5.5 months old and following a 6-hr sleep deprivation and found a significant but subtle sleep fragmentation (Figure S6H–J). *Bmal1* loss during adolescence led to 32% shorter and 44% more frequent wake events during the dark/active phase at baseline (Figure S6H–J **left**). However, unlike knocking out *Bmal1* embryonically, when *Bmal1* was lost during adolescence, sleep deprivation did not lead to changes in total time awake nor in NREM sleep (Figure S6H, K **right**). Moreover, the amount of dark phase NREM events was higher only following sleep deprivation but not at baseline, while the average duration was not affected in either condition (Figure S6L–M). These results suggest oligodendroglial lineage cells play a role during early-life brain development in not only the establishment of oligodendroglial densities but also the sleep network, with NREM-mediated sleep fragmentation being more prominently impacted following embryonic oligodendroglial dysregulation. These results confirm sleep fragmentation in OPC-specific BMAL1 knockout models using both *NG2:Cre* and *PDGFRα::CreER*^{T2} mice.

The remyelination potential of oligodendroglial lineage cells depends on functional BMAL1 during adulthood

We next investigated if *Bmal1* loss in adulthood led to baseline deficits in OPC dynamics as identified above following early-life disruption. To evaluate the effect of *Bmal1* loss during adulthood, *PDGFRα::CreER*^{T2};*Bmal1*$^{fl/fl}$ mice were injected intraperitoneally with 100 mg/kg tamoxifen for 3 consecutive days at 3 months and brains were evaluated 6 weeks later. We found that OPC density was no longer decreased as with embryonic or adolescent knock out, but morphological complexity was still reduced with *Bmal1* loss in adulthood (Figure 6A).

As regulation of OPC population density depends on OPC morphology, we next assessed whether these morphological changes affected remyelination. We generated a unilateral focal demyelinating lesion in the corpus callosum with stereotactic injection of lysolecithin 6 weeks after tamoxifen injections at 3 months of age in OPC-*Bmal1*-iKO and OPC-*Bmal1*-WT mice (Figure 6B–C). Lysolecithin-induced lesions progress from an active demyelination phase during the first 3 days, to OPC recruitment (days 3 to 7), differentiation (days 7 to 10), and active remyelination (days 10 to 21).[50] When *Bmal1* knock out and demyelination occur in adulthood, intra-lesion OPC density 5 days post-lysolecithin injection (dpi) compared to the non-lesioned hemisphere was significantly lower in OPC-*Bmal1*-iKO than OPC-*Bmal1*-WT mice. This difference was not attributed to OPC proliferation changes (Figure 6D–E). By 9 dpi the OPC density difference no longer existed between genotypes, but the density of lesion-associated oligodendrocytes compared to the non-lesioned hemisphere was significantly decreased in OPC-*Bmal1*-iKO compared to OPC-*Bmal1*-WT mice (Figure 6F–G). Twenty days after demyelination, remyelination of small caliber axons was reduced in OPC-*Bmal1*-iKO compared to WT mice (Figure 6H–I), suggesting that the ability of OPCs to dynamically respond to a demyelinating lesion and properly remyelinate is impacted by BMAL1 status.

Sleep fragmentation is linked with increased risk of multiple sclerosis

Given that our above mouse models with irregular maintenance of oligodendroglia exhibit increased sleep fragmentation and deficient remyelination potential, could changes in sleep fragmentation be associated with demyelinating disorders in humans? We evaluated the association between changes in sleep and risk of the demyelinating disorder MS. We performed Mendelian randomization (MR) analyses on lead variants identified in a GWAS of sleep fragmentation (defined as number of sleep episodes) in 85,723 individuals in the UK Biobank[51] and 339,015 individuals in FinnGen. We evaluated their association with MS risk by leveraging results from a GWAS of MS in the International Multiple Sclerosis Genetics Consortium (N = 47,429 MS patients and 68,374 controls) (Table S4).[52] Eleven variants associated with number of sleep episodes/sleep fragmentation were suitable for MR analysis after exclusions (Table S4). We identified that sleep fragmentation was associated with an increased risk of MS (UK BioBank: Inverse Variance Weighted OR = 1.11 [CI=1.01–1.23], $P = 0.034$, per unit increase in the number of sleep episodes, 95%; Figure 6J–K; FinnGen: Inverse Variance Weighted OR = 1.19 [1.03–1.38], $P = 0.017$, 95%; Figure S6N–O). Furthermore, MR Egger analysis, which estimates the total pleiotropic effect of the variants used, showed no significant pleiotropy (UK BioBank; MR Egger Intercept $P = 0.32$; Figure 6J–K; FinnGen: MR Egger Intercept $P = 0.68$; Figure S6N–O). Taken together, these findings indicate a previously underappreciated link between aberrant sleep fragmentation and myelin disease in humans.

Discussion

How OPCs balance the timing of proliferation and differentiation to maintain even tiling within the CNS remains incompletely understood. Here, we establish that BMAL1 is necessary for proper OPC lineage maintenance and subsequent myelin formation throughout development, adulthood, and injury. These decrements are associated with deficiencies in motor and cognitive function and sleep architecture. The sleep fragmentation characterized in mice lacking OPC-specific BMAL1 is exacerbated by sleep deprivation, providing a *proof-of-concept* that abnormal myelin-forming cell maintenance dysregulates sleep architecture and homeostatic recovery. We also found sleep fragmentation in humans is associated with MS risk, although the mechanisms driving this association remain to be fully determined. Collectively, these findings link BMAL1 with homeostatic regulation of oligodendroglia in development and disease.

Our results suggest that these myelin-associated changes following BMAL1 loss are related to deficiencies in OPC population establishment in specific brain regions during early development, exemplified by reduced proliferative and migratory capacity and diminished gene expression of cell cycle, proliferation, cytoskeletal and migratory regulators. This is particularly interesting given the remarkable ability of OPCs to evenly space throughout the CNS.[3] The timing mechanisms that allow for the precise orchestration of OPC proliferation and differentiation to maintain this homeostatic density remain to be fully determined, but previous work has implicated factors like Id2, a known circadian clock regulator[53] that cycles in OPCs and is downregulated in OPCs with BMAL1 loss. Transcripts that control OPC proliferation increase during the sleep/light phase,[17] a period when *Bmal1* peaks in mice. Recent work further supports the role of BMAL1 in OPC proliferation during late adolescence, with significant decreases in proliferating OPCs following BMAL1 loss in mice.[54] Future work focused on disrupting other clock genes will help discern BMAL1 circadian vs non-circadian mechanisms on temporal OPC dynamics.

We find that BMAL1 robustly regulates OPCs during embryonic and early postnatal life, when developmental OPC establishment, oligodendrogenesis and myelination are occurring,[55] but its role in OPC maintenance decreases throughout adulthood. As BMAL1 regulates the OPC cell cycle, and the mitotic rate of OPCs decreases with age,[9] this finding further supports the role of BMAL1 in controlling OPC division during development. Previous work demonstrated that changes in astrocyte circadian clock within a demyelinating lesion signal suppression of subventricular zone BMAL1 and promotes oligodendrogenesis from neural precursor cells.[56] However, this work did not investigate the specific effect of BMAL1 loss on oligodendroglia in remyelination during adulthood. Our data presented here imply BMAL1 controls OPC morphology, migration and recruitment more so than proliferation following demyelination in adulthood, a critical step for remyelination[57] that is deficient in MS.[12] Decreased expression of the migratory factors *Bmp4*,[34] *Bmp7*,[34] *Tgfb1*[34] and *Cdk5*[33,58,59] and aberrant morphology and migration following OPC-specific BMAL1 loss further supports its role in migration. Interestingly, many of the genes downregulated in OPCs following BMAL1 loss, like *Cdkn1a, Ddit3*, *Tubb6*, *Cebpb*, *Btg1* and *Klf4*, map onto genes that are upregulated in OPCs within demyelinating lesions.[60] Future work identifying the role of circadian genes in oligodendroglia of individuals with MS is necessary.

Abnormal myelin and deficiencies in sleep and circadian biology are increasingly identified co-morbidities in a variety of progressive neurological disorders, including MS. Up to 60% of individuals with MS report sleep and circadian abnormalities[20] and genetic variability in *ARNTL/BMAL1*, *CLOCK*,[18] and *PER3*[61] are associated with increased risk of MS. Whether our identified changes in sleep are due directly to the function of BMAL1 in OPCs or if other factors that similarly dysregulate oligodendroglial maintenance or myelination can also disrupt sleep architecture remains to be fully investigated. Oligodendroglial lineage cells could modulate circuit function through mechanisms beyond myelination,[62] including OPC population synaptic integration[8] into neural circuitry and OPC sculpting of neural circuits through synaptic pruning,[63] and our gene expression data suggest that BMAL1 may regulate OPC synapses. Understanding exactly how these cells are integrated into the brain-wide sleep network will expand our understanding of neuron-glia interactions dictating sleep physiology.

Importantly, OPC-*Bmal1*-KO mice did not display the gross sleep loss during either the rest or active phases which is associated with both decreased myelin[64] and deficits in cognition using the novel object recognition task,[65] suggesting that the sleep circuit changes in our model are linked to sleep timing more so than sleep amount or sleep recovery. Our finding that sleep fragmentation is also associated with MS prevalence further supports the supposition that a relationship between myelin-forming cells and sleep may exist and indicates that sleep fragmentation may be a biomarker for MS as has been reported in Alzheimer's disease.[66,67] Whether this relationship is mechanistically driven by the myelin or immune phenotypes underlying MS pathophysiology requires further investigation. By defining the role of BMAL1 in oligodendroglial lineage cells throughout life, we have identified new mechanistic insights into myelin-forming cell regulation that may provide therapeutic targets for myelin-associated neurodegenerative disorders.

STAR Methods:

RESOURCE AVAILABILITY

Lead contact—Further information and requests for resources and reagents should be directed to and will be fulfilled by the lead contact, Dr. Erin M. Gibson (egibson1@stanford.edu).

Materials availability—This study did not generate new unique reagents.

Data and code availability

- The Multiple Sclerosis summary statistics are publicly available through TwoSampleMR package. To access individual-level data from the UK Biobank studies, researchers must apply for access through the UK Biobank portal at https://www.ukbiobank.ac.uk/enable-your-research/apply-for-access. The RNA-seq datasets have been deposited in Gene Expression Omnibus (GEO) and GEO accession numbers are reported in the key resources table.
- This paper does not report original code.
- Any additional information required to reanalyze the data reported in this paper is available from the lead contact upon request.

EXPERIMENTAL MODEL AND SUBJECT DETAILS

Animal Procedures and Mouse Models—All procedures were performed in accordance with guidelines set in place by the Stanford University Institutional Care and Use Committee. Mice were housed in group cages, except for mice that received surgical procedures, according to standard guidelines with *ad libitum* access to food and water under a 12::12 hr light/dark cycle. Both sexes were equally used in all experiments to ensure claims included data from both male and female mice. However, we cannot make any direct claims about the influence of sex on our findings as we are underpowered for most of our analyses based on sex. *NG2::Cre* and *PDGFRα*::*CreER*^{T2} were bred with *Bmal1*$^{fl/fl}$ mice (The Jackson Laboratory 008533, 018280, 007668) to produce *NG2::Cre;Bmal1*$^{fl/fl}$ and *PDGFRα::CreER*^{T2}*;Bmal1*$^{fl/fl}$ conditional constitutive and inducible knock out models, respectively. B6.129S6-*Per2*^{tm1Jt}/J mice (The Jackson Laboratory 006852) were bred for OPC isolation for *in vitro* bioluminescence assays. Genotyping was performed by PCR using genomic DNA extracted from ear or toe biopsies. Primers used for genotyping are listed in Table S5. *PDGFRα::CreER*^{T2}*;Bmal1*$^{fl/fl}$ mice were intraperitoneally (IP) injected with 100 mg/kg tamoxifen (Sigma T5648) for 3 consecutive days at P18–20 (adolescence) or 3 months (adulthood) of age. For OPC proliferation assessment, 40 mg/kg EdU (5-ethynyl-2’-deoxyuridine, Invitrogen E10187) was IP injected either for 3 consecutive days before perfusions (for genotypes comparisons) or on a single pulse 30 min before perfusions (for ZT0 vs ZT12 comparisons).

METHOD DETAILS

Lysolecithin Demyelination Model—Lysolecithin (L-α-Lysophosphatidylcholine, Sigma L4129) was diluted to 1% in sterile 1x phosphate-buffered saline (PBS), and aliquots were frozen at −20°C for single use. Six weeks after tamoxifen injections, *PDGFRα::CreER*^{T2}*;Bmal1*$^{fl/fl}$ mice were anesthetized with 3.5–5% isoflurane and placed in a stereotactic apparatus. Isoflurane was maintained at 1.5–3.0% throughout the procedure. The cranium was exposed via midline incision under aseptic conditions and a hole was drilled in the skull for injection at the following coordinates: +1.0 anterior to bregma, +1.0 lateral to midline, +1.4 dorsal to ventral. A blunt-tip 26s-gauge Hamilton syringe was used to inject 2μl of 1% lysolecithin into the cingulum of the corpus callosum of one hemisphere using a digital pump at infusion rate of 0.2 μl/min. At the completion of infusion, syringe needle remained in place for a minimum of 5 min to minimize backflow of the injection. Mice were administered bupivacaine prior to first incision, and carprofen and 0.9% sodium chloride upon completion of sutures. Mice were monitored post-operatively daily until perfused.

Telemetry Implantation and Locomotor Recording—To measure locomotor activity, 2-month old *NG2::Cre;Bmal1*$^{fl/fl}$ and *PDGFRα::CreER*^{T2}*;Bmal1*$^{fl/fl}$ mice were implanted with a telemetry device (G2 E-Mitter, Mini Mitter OR, USA) in the abdominal cavity under 3% isoflurane anesthesia. Mice were allowed to recover for 3 weeks. Locomotor activity was telemetrically monitored in 12::12 light/dark (LD) cycles for 7 days followed by constant darkness (DD) for 15 days. Locomotor activity was monitored through VitalView software (Mini Mitter, OR, USA) and analyzed in 1 hr bins.

Electroencephalogram (EEG)/ Electromyogram (EMG) Surgery and Sleep Recordings—To evaluate sleep, a headstage with 4 EEG and 2 EMG electrodes on the skull was surgically implanted under 3% isoflurane anesthesia in 3.5-month old mice. Two EEG electrodes were screwed over the motor cortex (±1 mm lateral and 1 mm anterior to bregma) and the other two electrodes over the visual cortex (±3 mm lateral and 1 mm anterior to lambda). Two Teflon-coated stainless-steel wires for EMG were placed into the neck extensor muscles. At 5 months of age, mice were tethered to recording cables that connect to a low-torque slip-ring commutator (Biella Engineering, Irvine, CA, USA). After 1 week of habituation to the cable and recording environment, EEG/EMG activity was recorded for 10 days. Mice were then sleep deprived for 6 hrs, and sleep waves were recorded for 12 hrs post sleep deprivation.

EEG and EMG signals were acquired using a Glass amplifier (West Warwick, RI, USA), filtered (30 Hz Low Pass Filter for EEG; 10–100 Hz Band Pass Filter for EMG) and captured at a sampling rate of 128 Hz using a sleep recording system (Vital Recorder; Kissei Comtec Co. Ltd., Matsumoto, Japan). EEG and EMG signals were automatically scored in 10 s epochs using SleepSign software (Kissei Comtec Co. Ltd., Matsumoto, Japan). According to standard criteria, each epoch was classified as Wake, NREM, or REM sleep.

The automatic scoring output was visually examined and confirmed by an experienced scorer, blind to genotype. Fast Fourier transform (FFT) was performed to analyze power spectra profiles of EEG over a 0–30 Hz with 0.5 Hz bins for the δ (0.5–4 Hz) and θ (4–9 Hz) bandwidths in a state-specific manner. A relative EEG power spectrum was calculated from EEG power densities in each frequency bin and normalized by the total bandwidth over 0–30 Hz. Epochs with artifacts and noise were excluded from the calculation.

Behavioral Tests—Motor function was tested using a CatWalk gait analysis system (Noldus, Netherlands). Mice were acclimated to handling before recording but no training was performed on the CatWalk apparatus prior to testing. Testing was performed in a dark room with red light during the light phase. Runs were considered successful when mice performed a consistent movement lasting no more than 5 s. All the analysis was performed on the CatWalk XT 9.0 software using four successful runs per mice. Swing speed was defined as the speed (cm/s) of the paw during limb swinging. It was calculated as the average of left and right forepaw swing speeds. Stride length was defined as the distance (cm) between successive placements of the same paw in the glass blade from one step cycle until the same paw touches the blade in the next cycle. It was calculated based on the X-coordinates of the center of the paw during maximum contact of the paw with the glass blade.

To specifically target frontal lobe-associated short-term memory and attention rather than long-term memory and hippocampal function in mice, a modified version of the novel object recognition task (NORT) was implemented.[41,43] Mice were handled for 2 minutes daily for the duration of the week leading up to the test. Mice were placed in the experimental chamber to acclimatize for 20 min the day before testing. Opaque Plexiglas experimental chambers of 61cm × 61cm × 61cm size, and a camera mounted 115 cm above the chamber were used. The tests were conducted during the first half of the animal’s light phase, in a room dimly lit by standing lamps aimed away from apparatus to provide diffuse light. On the day of testing, mice were handled for 2 min before acclimatizing for 20 min in the empty chamber. Mice were returned to their home cages for 5 min before being placed in the experimental chamber with either 2 identical Lego objects (of approx. 12 cm in height) or 2 identical opaque mini bottles approximately the same width and height as the Lego-objects to counterbalance the use of each object. The position of the novel object from trial to trial was also counterbalanced. Objects were randomly assigned to avoid bias. Objects were secured in the center of the arena, 10 cm from the sidewalls and mice were placed in the center of the chamber between the 2 objects, facing perpendicular to the objects. During the training phase, mice were allowed to explore the identical objects for 5 min before being returned to their cages for 5 min while objects were cleaned with 70% ethanol. One of the 2 objects was then replaced with a new, cleaned un-identical object. During the testing phase, mice were again placed at the center of the chamber between both objects and facing perpendicular to both objects. During this phase, mice were allowed to explore for 10 min. Trials were recorded using Ethovision XT (Noldus Information Technology, Wageningen, the Netherlands) and interactions were scored by a researcher blinded to all conditions. Interactions with each object are defined as sniffing, biting and/or head within 2 cm of object, but not casually touching the object in passing or climbing. Only animals that explored the objects for a minimum of 10 s were included in the analysis.

Perfusions, Immunofluorescence and Confocal Imaging—P0 mouse brains were fixed in 4% paraformaldehyde (PFA) for 4 hr at 4°C, and then cryoprotected in 30% sucrose. P21 and adult mice were anesthetized using lethal dose of Avertin (tribromoethanol, Sigma T48402) and transcardially perfused with 15 ml PBS using a peristaltic pump (VWR 70730–062). All mice were perfused during the rest phase at Zeitgeber time (ZT)5–9 (ZT0=lights on; ZT12=lights off), with all experimental and control mice perfused at the same ZT. Brains were fixed in 4% PFA overnight at 4°C, and then cryoprotected in 30% sucrose. Forty μm coronal sections were taken using a sliding microtome (Epredia HM450 22-050-856) for P21 and adult brains and using a sliding cryostat (Leica CM 1850; Leica Biosystems, Wetzlar, Germany) for P0 brains. For immunohistochemistry involving EdU, sections were stained using Click-iT EdU cell proliferation kit and protocol (Invitrogen C10339) followed by incubation in 3% normal donkey serum with 0.3% Triton X-100/TBS blocking solution at room temperature for 1 hr and then incubated overnight at 4°C with primary antibodies. For all other stains, sections were incubated directly in blocking solution at room temperature for 1 hr and then incubated overnight at 4°C with primary antibodies. Goat anti-PDGFRα (1:500; R&D Systems AF1062), mouse anti-CC1 (1:20; EMD Millipore OP80), rabbit anti-BMAL1 (1:500, Novus Biologicals NB100–2288), chicken anti-TH (1:2000, Aves lab AB_10013440), goat anti-CD31 (1:500, R&D Systems AF3628), rat anti-CD13 (1:500, Biorad MCA2183), and rat anti-MBP (1:500; Abcam ab7349) were diluted in 1% normal donkey serum in 0.3% Triton X-100 in TBS. CC1 was incubated for 7 days at 4°C as previously described [6]. Sections were then rinsed three times in 1X TBS and incubated overnight at 4°C in secondary antibody diluted to 1:500 in 1% normal donkey serum with 0.3% Triton X-100/TBS. The secondary antibodies used include: Alexa 488 sheep anti-mouse IgG, (Jackson Immunoresearch 515-545-072), Alexa 594 donkey anti-mouse IgG, (Jackson Immunoresearch 715-585-150), Alexa 647 donkey anti-mouse IgG, (Jackson Immunoresearch 715-605-150), Alexa 488 donkey anti-rabbit IgG (Jackson Immunoresearch 711-546-152), Alexa 594 donkey anti-rabbit IgG (Jackson Immunoresearch 711-586-152), Alexa 647 donkey anti-rabbit IgG (Jackson Immunoresearch AB_2492288), Alexa 488 donkey anti-goat IgG, (Jackson Immunoresearch 705-545-147), Alexa 594 donkey anti-goat IgG (Jackson Immunoresearch 705-586-147), Alexa 647 donkey anti-goat IgG (Jackson Immunoresearch 705-606-147), Alexa 488 donkey anti-rat IgG (Jackson Immunoresearch 712-545-153), Alexa 594 goat anti-rat IgG (Jackson Immunoresearch 112-005-167), Alexa 647 donkey anti-rat IgG (Jackson Immunoresearch 712-586-150). The next day, sections were rinsed 3 times in TBS, incubated with DAPI for 5 min (1:1000; Thermo Fisher Scientific 62247) and mounted with ProLong Gold mounting medium (Life Technologies P36930). Secondary-only stains were performed as negative controls. Sections were imaged using a confocal microscope (Zeiss LSM900). Images were taken at 10X, 20X or 40X magnification according to the experiment and analyzed using Zen software. Z-stacks were acquired, and a maximum intensity image was generated for each frame.

Transmission Electron Microscopy—Mice under anesthesia with a lethal dose of Avertin were sacrificed by transcardial perfusion with 10 mL PBS followed by 10 mL

Karnovsky’s fixative: 2% glutaraldehyde (EMS 16000) and 4% paraformaldehyde (EMS 15710) in 0.1 M sodium cacodylate (EMS 12300), pH 7.4. A region containing premotor cortex and corpus callosum was resected from the brain and post-fixed in Karnovsky’s fixative for at least 2 weeks. The effect on myelination due to OPC-specific *Bmal1* loss was measured by transmission electron microscopy of axial sections in the region of the premotor projections entering the corpus callosum at the level of the cingulum, while post-injury remyelination was measured on sagittal sections of the corpus callosum at 600 μm lateral to the lesion epicenter. First, samples were post-fixed in a solution of 2% osmium tetroxide (EMS 19100) for 5 hr at 4°C, washed 3 times with ultrafiltered water, then en bloc stained with 1% uranyl acetate overnight at room temperature and dehydrated in ethanol (30%, 50%, 70%, and 95%) for two rounds of 10 mins each at room temperature, followed by 10 minutes in 100% ethanol at 4°C, and a final step of 10 mins in propylene oxide at room temperature. Samples were infiltrated with increasing concentrations of the epoxy resin EMbed-812 (EMS 14120) at room temperature, beginning with 1 hr in 1:2 with EMbed-812:propylene oxide, followed by 1 hr in 1:1 Embed-812:propylene oxide, then overnight in 2:1 EMbed-812:propylene oxide, then 4 hrs in pure EMbed-812. Samples were then set in TAAB capsules filled with fresh Embed-812 and left at 65°C overnight. Sections were cut at 80 nm thickness on a Leica Ultracut S (Leica, Wetzlar, Germany) and mounted on Formvar/carbon coated slot grids (EMS FCF2010-Cu) or 100 mesh Cu grids (EMS FCF100-Cu). Grids were contrast stained for 30 sec in 3.5% uranyl acetate in 50% acetone followed by staining in 0.2% lead citrate for 2 mins. Samples were imaged using a JEOL JEM-1400 TEM at 120kV and images were collected using a Gatan Orius digital camera. g-ratios were measured by dividing the axonal diameter by the diameter of the entire fiber (diameter of axon/diameter of axon + myelin sheath) at 8000X using ImageJ software blinded to genotype and condition. For each animal, 100 axons were scored. Statistical analyses were calculated using the mean g-ratio per mouse, with each mouse representing one data point. Scatter plots were performed using g-ratios as function of axon calibers of all the axons analyzed.

Blood-brain Barrier Permeability—At ZT10.5, mice were injected IP with 25 mg/kg NaFl (Sigma 46960) and, after 90 minutes, anesthetized with a lethal dose of Avertin. Blood from the right ventricle was extracted with a 23G needle and added into an EDTA-coated tube. Mice were then perfused with PBS at 8 ml/min using a peristaltic pump (VWR 70730–062) before the frontal cortex and cerebellum were micro-dissected. Blood was centrifuged to collect plasma supernatant and then diluted 1:10 in sterile PBS followed by an additional 1:1 dilution in 2% Trichloroacetic Acid (TCA). Tissue was homogenized in 1mL of PBS per 150 mg of tissue and centrifuged. Supernatants were then diluted 1:1 in 2% TCA. Both sets of samples were centrifuged, and supernatants were diluted 1:1 in borate buffer, pH 11 and fluorescence of the diluted supernatants was measured (SpectraMax iD3, excitation 480, emission 538). To ensure measurements were within detectable limits, a standard curve and blanks were used. Standards were performed with serial dilutions of lysates 0.5% TCA and 50% borate buffer in PBS with serial dilutions of sodium fluorescein dye. Blanks were 0.5% TCA and 50% borate buffer in PBS with no sodium fluorescein dye. Fluorescence ratios of brain lysates and blood samples were calculated for each mouse by taking the average of 3 technical replicates.

OPC Isolation from Mouse Brains for Culture—Mouse pups from both sexes were sacrificed at P6 and brains were enzymatically and mechanically dissociated as described.[68] OPCs were purified using immunopanning through 2 negative selection plates for microglia and endothelial cells with BSL1 (Vector Laboratories L1100) and one positive selection plate with an anti-PDGFRα antibody (rat anti-mouse CD140A, BD Pharmingen 558774) as described.[68] OPCs were seeded in Poly-D-lysine coated plates (Sigma P6407) and incubated at 37°C, 10% CO2 in DMEM-Sato base growth medium composed of Dulbecco's Modified Eagle's Medium (Invitrogen 11960–044), 100 U/mL penicillin and 100 μg/mL streptomycin (Gibco/Life Technologies 15140–122), 2 mM Glutamine (Invitrogen 25030–081), 1 mM Sodium pyruvate (Invitrogen 11360–070), 5 μg/mL Insulin (Sigma-Aldrich I6634), 5 μg/mL N-Acetyl-L-cysteine (Sigma-Aldrich A8199), 1x Trace Elements B (Corning 25022CI), 10 ng/mL d-Biotin (Sigma-Aldrich B4639), 100 μg/mL BSA (Sigma-Aldrich A4161), 100 μg/mL Transferrin (Sigma-Aldrich T1147), 16 μg/mL Putrescine (Sigma-Aldrich P5780), 60 ng/mL Progesterone (Sigma-Aldrich P8783), 40 ng/mL Sodium selenite (Sigma-Aldrich S5261), 4.2 μg/mL Forskolin (Sigma-Aldrich F6886) and 10 ng/mL CNTF (Peprotech 450–13). To promote OPC proliferation, cells were maintained in 10 ng/mL PDGF-AA (Peprotech 100–13A) and 1 ng/mL NT-3 (Peprotech 450–03). To promote OPC differentiation, cells were maintained in 1x B-27 (Invitrogen 17504–044) and 40 ng/mL T3 (Sigma-Aldrich T6397). Half of the media was replaced with fresh media every 2 days.

OPC Immunofluorescence—OPCs were seeded in ethanol-washed glass coverslips coated with Poly-D-lysine (Sigma P6407) in a density of 5000 cells/well in proliferation or differentiation media. For analyzing OPC proliferation, OPCs were incubated with 10μM EdU for 5 hrs and cells were then fixed in 4% PFA for 15 min at room temperature. For EdU staining, sections were permeabilized with 0.1% Triton X-100 in PBS for 3 min at room temperature and stained using Click-iT EdU cell proliferation kit and protocol (Invitrogen C10339) followed by an incubation with 3% BSA in PBS for 20 min at room temperature. For differentiation assays, after 3 or 6 days of OPCs incubation with differentiation factors, cells were fixed in 4% PFA for 15 min at room temperature, permeabilized with 0.1% Triton X-100 in PBS for 3 min at room temperature followed by an incubation with 3% BSA in PBS for 20 min at room temperature. Rat anti-MBP (1:500; Abcam ab7349), rabbit anti-BMAL1 (1:500, Novus Biologicals NB100–2288), goat anti-PDGFRα (1:500; R&D Systems AF1062) or rabbit anti-NG2 (1:500, Millipore AB5320) were diluted in 3% BSA in PBS and incubated overnight at 4°C. The next day, coverslips were rinsed 3 times in PBS and incubated in secondary antibody solution in 3% BSA for 2 hr at room temperature. The following secondary antibodies were used at 1:500: Alexa 594 goat anti-rat IgG (Jackson Immunoresearch 112-005-167), Alexa 488 donkey anti-rabbit IgG (Jackson Immunoresearch 711-546-152), Alexa 488 donkey anti-goat IgG (Jackson Immunoresearch 705-545-147), Alexa 594 donkey anti-rabbit IgG (Jackson Immunoresearch 711-586-152). Coverslips were rinsed 3 times in PBS, incubated with DAPI for 10 min (1:1000; Thermo Fisher Scientific 62247) and mounted with ProLong Gold mounting medium (Life Technologies P36930). For differentiation assays, Phalloidin (1:143 of 66 μM stock, Invitrogen A12379) was also added to the DAPI solution to stain F-actin to distinguish the differentiation stage as previously described.[69] Secondary-only stains were performed as negative controls. Confocal Imaging and quantification were performed as previously stated for *in vivo* experiments on Z-stacks from 3×3 tiles taken at 10X.

Western Blot—Isolated OPCs were lysed with RIPA buffer containing protease inhibitors. Lysates were then centrifuged at 13,000g for 15 min at 4°C and total protein was quantified (Biorad 5000113 & 5000114). All samples were normalized by protein concentration, mixed with 1X Bolt DTT Reducing Agent (Invitrogen #B0009) and 1X Bolt LDS sample buffer (Invitrogen B0007), incubated at 70°F for 10 min, and loaded onto Bolt 4–12% Bis-Tris Plus (Invitrogen NW04120). Protein was semi-dry transferred at 20–25V onto nitrocellulose membranes (Invitrogen IB23002) and blocked with 5% bovine serum albumin (BSA Sigma #A3294) in TBST for 1h. Direct-blot™ HRP rat anti-GAPDH (1:1000, BioLegend 607903) and rabbit anti-BMAL1 (1:2000, Novus Biologicals NB100–2288) antibodies were diluted in 1% BSA/TBST and membranes incubated overnight at 4°C. The following day, membranes were rinsed 3 times in TBST and incubated with a secondary goat anti-rabbit IgG antibody conjugated to horseradish peroxidase (1:5000, VWR 10150732) for 1hr. Proteins were visualized using WesternBright Sirius (Advansta K-12043-C20) and quantified using Image Studio Lite software (LI-COR).

Luminescence Assays—To test OPC circadian synchronization *in vitro*, immunopan-isolated OPCs from B6.129S6-*Per2*^{tm1Jt}/J P6 mouse brains were seeded in 60000 cells/well in 96 well opaque plates. OPCs were treated with 100 nM dexamethasone (Sigma-Aldrich D4902) for 1 hr followed by a complete media change or synchronized using a media change containing 10 μM forskolin (Sigma-Aldrich F6886). Given the high mitotic rate of OPCs, OPCs synchronized with the dexamethasone were cultured in the presence of the antimitotic agent Aphidicolin (1 μg/mL, Sigma 178273) prior to bioluminescence measurements to avoid desynchronization due to high proliferation. At each circadian time (CT) in which bioluminescence was measured, 1 μM beetle luciferin potassium salt (Promega E1602) was added, and bioluminescence was recorded after 20 min in a SpectraMax iD3 plate reader. Measurements were taken for 48 hr and the first 12 hours were removed from the analysis.

RT-qPCRs—Clock gene expression was measured on primary cultures of OPCs isolated from P6 mouse brains and circadian synchronized *in vitro* using dexamethasone 100nM for 1 hr. Samples were collected at CT4, 8, 12, 16, 20 and 24 after *in vitro* synchronization, lysed with 500 μL QIAzol Lysis Reagent (Qiagen 79306) and stored at −80°C until RNA extraction. RNA extraction was performed following manufacturer’s instructions and RNA purity and concentration were assessed using a NanoDrop and checking 260/280 and 260/230 nm ratios. 600 ng of RNA were used for first-strand cDNA synthesis using Oligo-dT primers and SuperScript™ III First-Strand Synthesis System (Invitrogen 18080051). Samples diluted in 1:8 were run in triplicate in an Applied Biosystems QuantStudio™ 6 Flex Real-Time PCR System machine using Power Up SYBR Green Master Mix (Applied Biosystems A25776) following supplier’s protocol and a cycling program of 2 min at 50°C followed by 2 min at 95°C and 40 cycles of 95°C for 15 sec and 60°C for 1 min. Primers used are listed in Table S5. Melting curves were analyzed to confirm specificity of the PCR product. Relative quantification against *Gapdh* reference gene expression was done using the 2-ΔΔCT method.

In Vitro Migration—For OPC migration in wound assays, primary cultures of *NG2::Cre-;Bmal1*$^{fl/fl}$ and *NG2::Cre+;Bmal1*$^{fl/fl}$ OPCs isolated from P6 mouse brains were seeded onto 96-well plates at a density of 100000 cells/well. After 24 hr of recovery, OPCs were circadian synchronized *in vitro* using dexamethasone 100nM for 1 hr. At CT0, a scratch wound was generated by scratching the cell monolayer in a straight line with a p10 tip. Plates were transferred to an IncuCyte ZOOM live cell imaging system (Essen Bioscience) set at 37 °C, 10% CO2. Images were taken for 24 hr by phase contrast with the 10× objective. The area migrated was calculated by subtracting the area covered by OPCs at time 24hr vs time 0hr.

For OPC transwell migration assays, primary cultures of *NG2::Cre-;Bmal1*$^{fl/fl}$ and *NG2::Cre+;Bmal1*$^{fl/fl}$ OPCs isolated from P6 mouse brains were seeded onto 8.0 μm pore Boyden chambers (Corning CLS3422) previously coated with PDL in 24-well plates at a density of 100000 cells/well. The lower compartment contained OPC proliferation media with 10 ng/mL PDGF-AA and 1 ng/mL NT-3, whereas the upper compartment lacked both proliferating factors. After 24 hr, cells in the upper compartment were swabbed and boyden chamber inserts were fixed with 4% PFA for 20 min. Migrated cells in the side of the insert were stained with crystal violet cell stain solution (0.1% Crystal Violet, 10% methanol in distilled water) for 20 min and then inserts were washed 3 times with distilled water. Crystal Violet was dissolved with 10% acetic acid and absorbance was determined at 570 nm.

For both assays, migration was measured in the presence of the antimitotic agent Aphidicolin (1 μg/mL, Sigma 178273) to discard the confounder of proliferation differences between genotypes. Results were expressed relative to migration of control OPCs (*NG2::Cre-;Bmal1*$^{fl/fl}$).

RNA Sequencing and Gene Expression Analysis—OPC-*Bmal1*-WT and OPC-*Bmal1*-KO mice mouse pups from both sexes were sacrificed at P6–7 and brains were enzymatically and mechanically dissociated as described.[68] For each biological replicate, 2 mice were pooled to obtain around 1×10^6 OPCs. OPCs were isolated at 4 different ZTs (ZT0, ZT6, ZT12, and ZT18). OPCs were purified using immunopanning through 2 negative selection plates for microglia and endothelial cells with BSL1 (Vector Laboratories L1100) and one positive selection plate with an anti-PDGFRα antibody (rat anti-mouse CD140A, BD Pharmingen 558774) as described.[68] One million cells were immediately lysed using QIAzol Lysis Reagent. RNA extraction was performed following manufacturer's instructions and RNA purity, integrity and concentration were assessed using a Bioanalyzer.

Library prep and Bulk RNA sequencing was performed using Novogene Co., Ltd. sequencing service. Messenger RNA was purified from total RNA using poly-T oligo-attached magnetic beads. After fragmentation, the first strand cDNA was synthesized using random hexamer primers, followed by the second strand cDNA synthesis using NEBNext Ultra II RNA Library Prep kit. The library was checked with Qubit and real-time PCR for quantification and bioanalyzer for size distribution detection. Quantified libraries were pooled and sequenced on NovaSeq 6000 S4 system and paired-end reads were generated. All libraries had > 80 million reads.

Index of the reference genome was built using Hisat2 v2.0.5 and paired-end clean reads were aligned to the mouse reference genome (GRCm38/mm10) using Hisat2 v2.0.5. FeatureCounts v1.5.0-p3 was used to count the reads numbers mapped to each gene. FPKM of each gene was calculated based on the length of the gene and reads count mapped to this gene. FPKM, expected number of Fragments Per Kilobase of transcript sequence per Millions base pairs sequenced, considers the effect of sequencing depth and gene length for the reads count at the same time, and is currently the most commonly used method for estimating gene expression levels. R-squared values of log-transofrmed FPKMs between biological replicates were generally around 0.93 (Figure S5A–B). Differential expression analysis was performed using the DESeq2 R package (1.20.0).[70] The resulting P values were adjusted using the Benjamini and Hochberg's approach[71] for controlling the false discovery rate. Genes with an adjusted P value < 0.05 found by DESeq2 were assigned as differentially expressed. Gene Ontology (GO) enrichment analysis of differentially expressed genes was implemented by the cluster Profiler R package, in which gene length bias was corrected. GO terms with corrected P value < 0.05 were considered significantly enriched by differential expressed genes. The Reactome database brings together the various reactions and biological pathways of human model species. Reactome pathways with corrected P value < 0.05 were considered significantly enriched by differential expressed genes. Heat maps of DEG were made using NovoMagic, a free Novogene platform for data analysis. To identify rhythmic expressed genes, JTK Cycle analysis[72] was performed using Nitecap.[73] Only genes with > 10 raw counts were used as inputs. Transcripts with adjusted JTK P value < 0.05, < 0.1 or < 0.2 were considered with strong, weak or weakest rhythmicity, respectively. Heat maps for rhythmic genes were made using Nitecap.

Mendelian Randomization (MR) Analyses—MR analyses were performed using genetic variants previously reported to be associated with multiple sclerosis,[52] and instruments from the mean number of sleep episodes per sleep period (a proxy for sleep fragmentation),[51,74] which was measured through wrist-worn accelerometer devices. All variants were first corrected for Winner's Curse[75,76] using a previously described method,[77] as Winner's Curse leads to an overestimation of the effect of the genetic instruments on the exposure and, in MR, can bias the causal effect towards the null.[78] Of the 21 lead variants available for sleep fragmentation, two were unavailable in the MS summary statistics and further eight were excluded due to being weak instruments after Winner's Curse correction (Table S4).

The Mendelian randomization framework is essentially akin to a randomized control trial where genetic risk of the exposure (in this case fragmented sleep) is randomized at conception. The idea behind MR is that if an exposure truly has a causal impact on an outcome (in this case sleep fragmentation on MS risk) then genetic variants that are associated with the exposure (sleep fragmentation) will also show a systematic effect on the outcome, which will be a function of their effect on the exposure multiplied by the true causal impact of the exposure on the outcome. Therefore, by using genetic proxies for the exposure and seeing how they influence the outcome, we are estimating the **true causal**

effect of the exposure on the outcome and not the effect that comes from the genetics only (the MR framework is a special case of a wider family of analytical frameworks called Instrumental Variables Estimation). The MR framework requires that the genetic variants:

1. show strong and robust association with the exposure (in genome-wide association studies, we used a *P*-value threshold of 5×10^{-8});
2. do not show evidence of pleiotropy (affecting the outcome but not through the exposure) so we know that the genetic variants are influencing the outcome only through their effect on the exposure and;
3. are not associated with environmental factors that can affect both the exposure and the outcome, which can induce collider bias.

We satisfy requirement 1 by selecting variants associated with objective sleep fragmentation that pass a strict multiple-testing threshold of $P \leq 5\times10^{-8}$. We test for requirement 2 by performing sensitivity analyses with the MR framework (penalized weighted median and MR Egger) that are robust to the effects of pleiotropy - as these tests are typically very statistically low powered (within an already low-powered MR framework), it is sufficient to test if the estimated causal effect from the sensitivity analyses is consistent in direction and magnitude compared to the primary estimate (from the inverse-variance weighted MR analysis). Requirement 3 is automatically satisfied by the use of genetic variants as instrumental variables, as these are assigned at conception and do not “change” in response to changing environmental factors across the life course. By satisfying these requirements, we exclude the possibility of reverse causation (i.e. the effects of MS on sleep fragmentation). If needed, more information on the MR framework can be found here: https://www.bmj.com/content/362/bmj.k601.

Five MR approaches were used: inverse-variance weighted (IVW), Weighted median, Weighted mode, Simple mode and MR with Egger regression (MR Egger) using TwoSampleMR package version 0.5.6 with R version 4.1.3. IVW is the most statistically powerful of the three methods but assumes that all included instruments are non-pleiotropic.[79] The weighted median (WM) approach provides a causal estimate that is consistent even if up to half of the variants are invalid instruments (due to pleiotropy), with the caveat of a loss of statistical power.[80] The MR Egger approach loosens the requirement that all genetic variants satisfy the exclusion-restriction principal. In the context of MR, this allows a subset of variants to be pleiotropic and so adjusts the causal estimate for the estimated overall directional pleiotropy (represented by a constant term in the linear regression equation).[81] Power calculations were performed using the mRnd tool,[82] available at the website https://shiny.cnsgenomics.com/mRnd/, using the Binary Outcome calculator with the total sample size set as 115,803 (sample size of the Multiple Sclerosis consortium), alpha as 0.05 (default), the proportion of cases in the study as ˜0.69 (= 47429/68374), the true odds ratio as 1.17 (the Weighted median causal effect size estimate) and the proportion of variance explained as ~0.004674 (the sum of the variance explained by the 11 variants used in the MR analysis resulting 38% power to detect association with this alpha level; Table S4).

QUANTIFICATION AND STATISTICAL ANALYSIS

Cell counting was performed blinded to experimental conditions and genotype. Cells were considered co-labeled when two immunofluorescent markers co-localized in the same plane. For EdU stereology, all PDGFRα$^+$/EdU$^+$ cells were counted within the regions. The density of cells was determined by dividing the total number of PDGFRα$^+$/EdU$^+$ cells quantified for each lineage by the total volume of the imaged frames (mm^3). For each mouse, 6 pictures were taken in the frontal lobe corpus callosum, 6 pictures in the cortex, and 1 picture in each of the remaining regions analyzed, and all the cells were counted for each immunohistochemical marker analysis.

To measure the volume of the corpus callosum, the Cavalieri Estimator function on a MBF Bioscience StereoInvestigator version 11.01.2 was used. Twelve coronal sections throughout the frontal lobe region were stained with MBP antibody and, under a 10X objective, the Cavalieri Estimator probe was used to trace the corpus callosum using published mouse anatomical guides to determine the boundaries.

For analyzing OPC morphology, semi-automated quantification was performed on Imaris for Neuroscientists Cell Imaging Software ver. 9.8. Filament Tracer Tool kit was used to automatically identify PDGFRα signal in the 3D space of 20X images. The spatial location of the cell body and processes was performed using the Autopath algorithm with the following parameters: starting points of 12.0 μm of largest diameter, and seed point of 1.62 μm of thinnest diameter. Morphological complexity was defined as the ratio between the sum of branch points and filament length by filament volume [complexity = (branch points + filament length) / filament volume].

For analyzing BMAL1 immunofluorescence intensity at ZT0 vs ZT12, 9 coronal sections throughout the frontal lobe region were taken at 20X per mouse, including 6 sections for cortex and 3 sections for the corpus callosum. Semi-automated quantification was performed on Imaris for Neuroscientists Cell Imaging Software ver. 9.8. Surface Tool kit was used to automatically identify PDGFRα and BMAL1 signal in the 3D space of 20X images. The spatial location of the cell body was performed using the Autopath algorithm with the following parameters: starting points of 12.0 μm of largest diameter, and seed point diameter of 6 μm. BMAL1 mean intensity was measured in the masked PDGFRα+ surfaces.

For analyzing pericyte coverage in the cortex, 6 brain sections per mouse were imaged on a confocal microscope (Zeiss LSM900) at 20X magnification. Z-stacks were acquired, and a maximum projections intensity image was generated for each frame with the ZenBlue software. For each frame, 2 TIFF files were acquired: a single channel TIFF of CD13+ fluorescent signal and a single channel TIFF of CD31+ fluorescent signal. With the Fiji/ImageJ software, each TIFF was converted to an 8-bit file and auto-thresholded. The percent CD31+ area per image was determined by the Analyze Particles function and any remaining autofluorescence was removed with the Size Exclusion feature. The percentage of colocalized CD13+ and CD31+ area per image was calculated using the Colocalization plug-in developed by Pierre Bourdoncle of the Institut Jacques Monod (http://rsb.info.nih.gov/ij/plugins/colocalization.html) and the Analyze Particles function.

Pericyte coverage was defined as the percentage of colocalized CD13+ CD31+ area per image divided by the percentage of total CD31+ area per image.

For OPC density establishment in the P0 developing cortex, 5 pictures at 20X magnification were taken across the cortex and 1 picture was taken in the subventricular zone. PDGFRα$^+$ OPC densities across the cortex were analyzed for each mouse. For OPC density establishment in the P0 developing hypothalamus, 3 pictures at 20X magnification were taken lateral to the ventricular germinal zone and 1 picture was taken in the adjacent area of the third ventricular zone. PDGFRα$^+$ OPC densities adjacent to the third ventricular area across the tuberal hypothalamus were analyzed for each mouse.

For lysolecithin-induced demyelination studies, MBP staining was used to identify the demyelinated lesion epicenter. Two images within the lesioned area of the cingulum were taken at 20X magnification for quantification: one medial and one lateral to the demyelinated lesion epicenter. Quantification in the lesion epicenter was avoided to prevent confounds associated with needlestick injury and subsequent OPC proliferation and microglial reactivity. Cell counting was performed on Z-stacks as previously stated and analyzed using Zen software. The average cellular density of both sections was compared to the contralateral non-lesioned side. To calculate the percentage of axons with aberrant myelination, around 100 axons per mice were scored. The following type of axons were considered to have aberrant myelination: axon with fragmented myelin ensheathed by at least some myelin at all points along circumference; axons with fragmented myelin such that axon is no longer ensheathed by at least some myelin at all points along circumference; and axons with no compact myelin.

All statistical analyses were conducted using GraphPad Prism statistical software, including Tests of Normality. Group mean differences between 2 genotypes for all immunofluorescence and Western blot analysis, morphological complexity, g-ratios, corpus callosum volume, CatWalk behavioral tests (swing speed and stride length), circadian period length, and locomotor activity were assessed using unpaired, two-tailed Student's t-tests. Group mean differences between genotypes in *in vitro* proliferation, differentiation and Boyden chamber migration assays were assessed using nested t-test to account for different experimental replicates. Bioluminescence was analyzed using One-way ANOVA with Holm-Sidak post-hoc tests to further examine pairwise differences. Group mean differences between 2 genotypes and different circadian times for proliferation, BMAL1 intensity and filament volume at ZT0 vs ZT12, and RT-qPCR of clock genes were compared with 2-way ANOVA with Holm-Sidak post-hoc tests to further examine pairwise differences. The rhythmicity of clock genes and bioluminescence of PER2:LUC cells was also analyzed using JTK cycle algorithm. Group mean differences between 2 genotypes and 2 conditions for NORT behavioral tests, sleep recordings, analysis of mean differences between the ipsilateral and contralateral sides within the same animal in the lysolecithin model, and blood-brain barrier permeability analysis were assessed with Two-way ANOVA with Holm-Sidak and Tukey post-hoc tests to further examine pairwise differences. A level of $P < 0.05$ was used to designate significant differences. Statistical details for each figure are included in Table S6.

Supplementary Material

Refer to Web version on PubMed Central for supplementary material.

Acknowledgments:

We would like to thank Drs. Richard Daneman and Caterina Profaci for their helpful guidance related to the assessment of the blood-brain barrier permeability. We would like to thank Drs. Tal Iram and William Giardino for their helpful comments on this manuscript. We acknowledge support from the U.S. Department of Defense (W81XWH-21-1-0846, EMG), the National Multiple Sclerosis Society (PP-1907-34759, RG-2205-39582, EMG), the Weintz Family COVID-19 Research Fund (EMG), the Department of Psychiatry and Behavioral Sciences, School of Medicine, Stanford University 2021 Innovator Grant Program (EMG), the Brain and Behavior Research Foundation NARSAD (AW905644, EMG), Brain Research Foundation (BRFSG-2022-04, EMG), the National Institutes of Health (R01 NS126610, EMG), the Maternal and Child Health Research Institute Postdoctoral Fellowship (DR), the Wu Tsai Neurosciences Institute Knight Initiative for Brain Resilience Scholar Award (DR), National Science Foundation Graduate Research Fellowship (DGE-1656518, CAG), Ford Foundation Predoctoral Fellowship (CAG), The National Cancer Institute, DHHS (PHS CA09302, LCM), BioX Institute Fellowship (JG, MEG, JR), The Instrumentarium Science Foundation (HMO), NIH Shared Instrumentation Grant (1S10RR02678001; Electron Microscopy Core at Stanford University Cell Sciences Imaging Facility). Research reported in this publication was also supported by the National Center for Advancing Translational Sciences of the National Institutes of Health under Award Number UL1TR003142 (EMG). The content is solely the responsibility of the authors and does not necessarily represent the official views of the National Institutes of Health.

References:

1. Hirrlinger J, and Nave K-A (2014). Adapting brain metabolism to myelination and long-range signal transduction. Glia 62, 1749–1761. 10.1002/glia.22737. [PubMed: 25130164]
2. Saab AS, Tzvetavona ID, Trevisiol A, Baltan S, Dibaj P, Kusch K, Möbius W, Goetze B, Jahn HM, Huang W, et al. (2016). Oligodendroglial NMDA Receptors Regulate Glucose Import and Axonal Energy Metabolism. Neuron 91, 119–132. 10.1016/j.neuron.2016.05.016. [PubMed: 27292539]
3. Dawson MRL, Polito A, Levine JM, and Reynolds R (2003). NG2-expressing glial progenitor cells: An abundant and widespread population of cycling cells in the adult rat CNS. Mol. Cell. Neurosci 24, 476–488. 10.1016/S1044-7431(03)00210-0. [PubMed: 14572468]
4. Matsumoto, Tsunekawa Y, Nomura T, Suto F, Matsumata M, Tsuchiya S, and Osumi N (2011). Differential Proliferation Rhythm of Neural Progenitor and Oligodendrocyte Precursor Cells in the Young Adult Hippocampus. PLoS ONE 6, 27628–27628. 10.1371/journal.pone.0027628.
5. Hughes EG, Kang SH, Fukaya M, and Bergles DE (2013). Oligodendrocyte progenitors balance growth with self-repulsion to achieve homeostasis in the adult brain. Nat. Neurosci 16, 668–676. 10.1038/nn.3390. [PubMed: 23624515]
6. Gibson EM, Purger D, Mount CW, Goldstein AK, Lin GL, Wood LS, Inema I, Miller SE, Bieri G, Zuchero JB, et al. (2014). Neuronal activity promotes oligodendrogenesis and adaptive myelination in the mammalian brain. Science 344, 1–27. 10.1126/science.1252304.
7. Rosenberg SS, Kelland EE, Tokar E, De La Torre AR, and Chan JR (2008). The geometric and spatial constraints of the microenvironment induce oligodendrocyte differentiation. Proc. Natl. Acad. Sci. U. S. A 105, 14662–14667. 10.1073/pnas.0805640105. [PubMed: 18787118]
8. Marisca R, Hoche T, Agirre E, Hoodless LJ, Barkey W, Auer F, Castelo-Branco G, and Czopka T (2020). Functionally distinct subgroups of oligodendrocyte precursor cells integrate neural activity and execute myelin formation. Nat. Neurosci 23, 363–374. 10.1038/s41593-019-0581-2. [PubMed: 32066987]
9. Spitzer SO, Sitnikov S, Kamen Y, Evans KA, Kronenberg-Versteeg D, Dietmann S, de Faria O, Agathou S, and Káradóttir RT (2019). Oligodendrocyte Progenitor Cells Become Regionally Diverse and Heterogeneous with Age. Neuron 101, 459–471.e5. 10.1016/j.neuron.2018.12.020. [PubMed: 30654924]
10. Viganò F, Möbius W, Götz M, and Dimou L (2013). Transplantation reveals regional differences in oligodendrocyte differentiation in the adult brain. Nat. Neurosci 16, 1370–1372. 10.1038/nn.3503. [PubMed: 23995069]

11. Kuhlmann T, Miron V, Cui Q, Cuo Q, Wegner C, Antel J, and Brück W (2008). Differentiation block of oligodendroglial progenitor cells as a cause for remyelination failure in chronic multiple sclerosis. Brain J. Neurol 131, 1749–1758. 10.1093/brain/awn096.
12. Boyd A, Zhang H, and Williams A (2013). Insufficient OPC migration into demyelinated lesions is a cause of poor remyelination in MS and mouse models. Acta Neuropathol. (Berl.) 125, 841–859. 10.1007/s00401-013-1112-y. [PubMed: 23595275]
13. Reddy AB, Wong GKY, O'Neill J, Maywood ES, and Hastings MH (2005). Circadian clocks: Neural and peripheral pacemakers that impact upon the cell division cycle. Mutat. Res. Mol. Mech. Mutagen 574, 76–91. 10.1016/j.mrfmmm.2005.01.024.
14. Ali AAH, Schwarz-Herzke B, Rollenhagen A, Anstötz M, Holub M, Lübke J, Rose CR, Schnittler HJ, and von Gall C (2020). Bmal1-deficiency affects glial synaptic coverage of the hippocampal mossy fiber synapse and the actin cytoskeleton in astrocytes. GLIA 68, 947–962. 10.1002/glia.23754. [PubMed: 31743496]
15. Gaucher J, Montellier E, and Sassone-Corsi P (2018). Molecular Cogs: Interplay between Circadian Clock and Cell Cycle. Trends Cell Biol 28, 368–379. 10.1016/j.tcb.2018.01.006. [PubMed: 29471986]
16. Laposky A, Easton A, Dugovic C, Walisser J, Bradfield C, and Turek F (2005). Deletion of the Mammalian Circadian Clock Gene BMAL1/Mop3 Alters Baseline Sleep Architecture and the Response to Sleep Deprivation. Sleep 28, 395–410. 10.1093/sleep/28.4.395. [PubMed: 16171284]
17. Bellesi M, Pfister-Genskow M, Maret S, Keles S, Tononi G, and Cirelli C (2013). Effects of sleep and wake on oligodendrocytes and their precursors. J. Neurosci 33, 14288–14300. 10.1523/JNEUROSCI.5102-12.2013. [PubMed: 24005282]
18. Lavtar P, Rudolf G, Maver A, Hodžić A, Starčević Čizmarević N, Živković M, Šega Jazbec S, Klemenc Ketiš Z, Kapović M, Dinčić E, et al. (2018). Association of circadian rhythm genes ARNTL/BMAL1 and CLOCK with multiple sclerosis. PLoS ONE 13, e0190601. 10.1371/journal.pone.0190601. [PubMed: 29324865]
19. Brzecka A, Leszek J, Ashraf GM, Ejma M, Ávila-Rodriguez MF, Yarla NS, Tarasov VV, Chubarev VN, Samsonova AN, Barreto GE, et al. (2018). Sleep Disorders Associated With Alzheimer's Disease: A Perspective. Front. Neurosci 12, 330. 10.3389/fnins.2018.00330. [PubMed: 29904334]
20. Sakkas GK, Giannaki CD, Karatzaferi C, and Manconi M (2019). Sleep Abnormalities in Multiple Sclerosis. Curr. Treat. Options Neurol 21, 4. 10.1007/s11940-019-0544-7.
21. Ehlen JC, Brager AJ, Baggs J, Pinckney L, Gray CL, DeBruyne JP, Esser KA, Takahashi JS, and Paul KN (2017). Bmal1 function in skeletal muscle regulates sleep. eLife 6, e26557. 10.7554/eLife.26557. [PubMed: 28726633]
22. Zhang Y, Chen K, Sloan SA, Bennett ML, Scholze AR, O'Keeffe S, Phatnani HP, Guarnieri P, Caneda C, Ruderisch N, et al. (2014). An RNA-sequencing transcriptome and splicing database of glia, neurons, and vascular cells of the cerebral cortex. J. Neurosci 34, 11929–11947. 10.1523/JNEUROSCI.1860-14.2014. [PubMed: 25186741]
23. Haque SN, Booreddy SR, and Welsh DK (2019). Effects of BMAL1 manipulation on the Brain's master circadian clock and behavior. Yale J. Biol. Med 92, 251–258. [PubMed: 31249486]
24. Krone LB, Yamagata T, Blanco-Duque C, Guillaumin MCC, Kahn MC, van der Vinne V, McKillop LE, Tam SKE, Peirson SN, Akerman CJ, et al. (2021). A role for the cortex in sleep-wake regulation. Nat. Neurosci 24, 1210–1215. 10.1038/s41593-021-00894-6. [PubMed: 34341585]
25. Altendahl M, Cotter DL, Staffaroni AM, Wolf A, Mumford P, Cobigo Y, Casaletto K, Elahi F, Ruoff L, Javed S, et al. (2020). REM sleep is associated with white matter integrity in cognitively healthy, older adults. PLOS ONE 15, e0235395. 10.1371/journal.pone.0235395. [PubMed: 32645032]
26. Ingram DG, and Churchill SS (2017). Sleep Problems in Children With Agenesis of the Corpus Callosum. Pediatr. Neurol 67, 85–90. 10.1016/j.pediatrneurol.2016.10.002. [PubMed: 28089768]
27. Avvenuti G, Handjaras G, Betta M, Cataldi J, Imperatori LS, Lattanzi S, Riedner BA, Pietrini P, Ricciardi E, Tononi G, et al. (2020). Integrity of Corpus Callosum Is Essential for theCross-Hemispheric Propagation of Sleep Slow Waves:A High-Density EEG Study in Split-Brain Patients. J. Neurosci. Off. J. Soc. Neurosci 40, 5589–5603. 10.1523/JNEUROSCI.2571-19.2020.

28. Nielsen T, Montplaisir J, and Lassonde M (1992). Sleep architecture in agenesis of the corpus callosum: laboratory assessment of four cases. J. Sleep Res 1, 197–200. 10.1111/j.1365-2869.1992.tb00038.x. [PubMed: 10607051]
29. Ono D, and Yamanaka A (2017). Hypothalamic regulation of the sleep/wake cycle. Neurosci. Res 118, 74–81. 10.1016/j.neures.2017.03.013. [PubMed: 28526553]
30. Saper CB, and Fuller PM (2017). Wake-Sleep Circuitry: An Overview. Curr. Opin. Neurobiol 44, 186–192. 10.1016/j.conb.2017.03.021. [PubMed: 28577468]
31. Chen VS, Morrison JP, Southwell MF, Foley JF, Bolon B, and Elmore SA (2017). Histology Atlas of the Developing Prenatal and Postnatal Mouse Central Nervous System, with Emphasis on Prenatal Days E7.5 to E18.5. Toxicol. Pathol 45, 705–744. 10.1177/0192623317728134. [PubMed: 28891434]
32. JTK_CYCLE: an efficient non-parametric algorithm for detecting rhythmic components in genome-scale datasets - PMC https://www-ncbi-nlm-nih-gov.stanford.idm.oclc.org/pmc/articles/PMC3119870/.
33. Miyamoto Y, Yamauchi J, and Tanoue A (2008). Cdk5 Phosphorylation of WAVE2 Regulates Oligodendrocyte Precursor Cell Migration through Nonreceptor Tyrosine Kinase Fyn. J. Neurosci 28, 8326–8337. 10.1523/JNEUROSCI.1482-08.2008. [PubMed: 18701695]
34. Choe Y, Huynh T, and Pleasure SJ (2014). Migration of Oligodendrocyte Progenitor Cells Is Controlled by Transforming Growth Factor β Family Proteins during Corticogenesis. J. Neurosci 34, 14973–14983. 10.1523/JNEUROSCI.1156-14.2014. [PubMed: 25378163]
35. Jablonska B, Adams KL, Kratimenos P, Li Z, Strickland E, Haydar TF, Kusch K, Nave K-A, and Gallo V (2022). Sirt2 promotes white matter oligodendrogenesis during development and in models of neonatal hypoxia. Nat. Commun 13, 4771. 10.1038/s41467-022-32462-2. [PubMed: 35970992]
36. Vieira N, Rito T, Correia-Neves M, and Sousa N (2021). Sorting Out Sorting Nexins Functions in the Nervous System in Health and Disease. Mol. Neurobiol 58, 4070–4106. 10.1007/s12035-021-02388-9. [PubMed: 33931804]
37. Li QS, and De Muynck L (2021). Differentially expressed genes in Alzheimer's disease highlighting the roles of microglia genes including OLR1 and astrocyte gene CDK2AP1. Brain Behav. Immun. - Health 13, 100227. 10.1016/j.bbih.2021.100227. [PubMed: 34589742]
38. A novel gene containing a trinucleotide repeat that is expanded and unstable on Huntington's disease chromosomes. The Huntington's Disease Collaborative Research Group (1993). Cell 72, 971–983. 10.1016/0092-8674(93)90585-e. [PubMed: 8458085]
39. Ferrari Bardile C, Garcia-Miralles M, Caron NS, Rayan NA, Langley SR, Harmston N, Rondelli AM, Teo RTY, Waltl S, Anderson LM, et al. (2019). Intrinsic mutant HTT-mediated defects in oligodendroglia cause myelination deficits and behavioral abnormalities in Huntington disease. Proc. Natl. Acad. Sci 116, 9622–9627. 10.1073/pnas.1818042116. [PubMed: 31015293]
40. Schöbel S, Neumann S, Hertweck M, Dislich B, Kuhn P-H, Kremmer E, Seed B, Baumeister R, Haass C, and Lichtenthaler SF (2008). A Novel Sorting Nexin Modulates Endocytic Trafficking and α-Secretase Cleavage of the Amyloid Precursor Protein. J. Biol. Chem 283, 14257–14268. 10.1074/jbc.M801531200. [PubMed: 18353773]
41. Gibson EM, Nagaraja S, Ocampo A, Tam LT, Wood LS, Pallegar PN, Greene JJ, Geraghty AC, Goldstein AK, Ni L, et al. (2019). Methotrexate Chemotherapy Induces Persistent Tri-glial Dysregulation that Underlies Chemotherapy-Related Cognitive Impairment. Cell 176, 43–55.e13. 10.1016/j.cell.2018.10.049. [PubMed: 30528430]
42. Nakazato R, Kawabe K, Yamada D, Ikeno S, Mieda M, Shimba S, Hinoi E, Yoneda Y, and Takarada T (2017). Disruption of Bmal1 Impairs Blood-Brain Barrier Integrity via Pericyte Dysfunction. J. Neurosci. Off. J. Soc. Neurosci 37, 10052–10062. 10.1523/JNEUROSCI.3639-16.2017.
43. Geraghty AC, Gibson EM, Ghanem RA, Greene JJ, Ocampo A, Goldstein AK, Ni L, Yang T, Marton RM, Paşca SP, et al. (2019). Loss of Adaptive Myelination Contributes to Methotrexate Chemotherapy-Related Cognitive Impairment. Neuron 103, 250–265.e8. 10.1016/j.neuron.2019.04.032. [PubMed: 31122677]

44. Carter ME, Yizhar O, Chikahisa S, Nguyen H, Adamantidis A, Nishino S, Deisseroth K, and de Lecea L (2010). Tuning arousal with optogenetic modulation of locus coeruleus neurons. Nat. Neurosci 13, 1526–1533. 10.1038/nn.2682. [PubMed: 21037585]
45. Osorio-Forero A, Cherrad N, Banterle L, Fernandez LMJ, and Lüthi A (2022). When the Locus Coeruleus Speaks Up in Sleep: Recent Insights, Emerging Perspectives. Int. J. Mol. Sci 23, 5028. 10.3390/ijms23095028. [PubMed: 35563419]
46. HIYOSHI H, TERAO A, OKAMATSU-OGURA Y, and KIMURA K (2014). Characteristics of Sleep and Wakefulness inWild-Derived Inbred Mice. Exp. Anim 63, 205–213. 10.1538/expanim.63.205. [PubMed: 24770646]
47. Vyazovskiy VV, and Delogu A (2014). NREM and REM Sleep: Complementary Roles in Recovery after Wakefulness. Neurosci. Rev. J. Bringing Neurobiol. Neurol. Psychiatry 20, 203–219. 10.1177/1073858413518152.
48. Zhu X, Bergles DE, and Nishiyama A (2008). NG2 cells generate both oligodendrocytes and gray matter astrocytes. Dev. Camb. Engl 135, 145–157. 10.1242/dev.004895.
49. Mount CW, Yalçın B, Cunliffe-Koehler K, Sundaresh S, and Monje M (2019). Monosynaptic tracing maps brain-wide afferent oligodendrocyte precursor cell connectivity. eLife 8, e49291. 10.7554/eLife.49291. [PubMed: 31625910]
50. Nait-Oumesmar B, Decker L, Lachapelle F, Avellana-Adalid V, Bachelin C, and Van Evercooren AB−. (1999). Progenitor cells of the adult mouse subventricular zone proliferate, migrate and differentiate into oligodendrocytes after demyelination. Eur. J. Neurosci 11, 4357–4366. 10.1046/j.1460-9568.1999.00873.x. [PubMed: 10594662]
51. Jones SE, van Hees VT, Mazzotti DR, Marques-Vidal P, Sabia S, van der Spek A, Dashti HS, Engmann J, Kocevska D, Tyrrell J, et al. (2019). Genetic studies of accelerometer-based sleep measures yield new insights into human sleep behaviour. Nat. Commun 10, 1585. 10.1038/s41467-019-09576-1. [PubMed: 30952852]
52. Patsopoulos NA, Baranzini SE, Santaniello A, Shoostari P, Cotsapas C, Wong G, Beecham AH, James T, Replogle J, Vlachos IS, et al. (2019). Multiple sclerosis genomic map implicates peripheral immune cells and microglia in susceptibility. Science 365. 10.1126/science.aav7188.
53. Wang S, Sdrulla A, Johnson JE, Yokota Y, and Barres BA (2001). A Role for the Helix-Loop-Helix Protein Id2 in the Control of Oligodendrocyte Development. Neuron 29, 603–614. 10.1016/S08966273(01)00237-9. [PubMed: 11301021]
54. Dean T, Koffi AV, Goldstein E, Ghaemmaghami J, and Gallo V (2022). Endogenous Circadian Clock Machinery in Cortical NG2-Glia Regulates Cellular Proliferation. eNeuro 9, ENEURO.0110–22.2022. 10.1523/ENEURO.0110-22.2022.
55. de Faria O, Pivonkova H, Varga B, Timmler S, Evans KA, and Káradóttir RT (2021). Periods of synchronized myelin changes shape brain function and plasticity. Nat. Neurosci 24, 1508–1521. 10.1038/s41593-021-00917-2. [PubMed: 34711959]
56. Huang S, Choi MH, Huang H, Wang X, Chang YC, and Kim JY (2020). Demyelination Regulates the Circadian Transcription Factor BMAL1 to Signal Adult Neural Stem Cells to Initiate Oligodendrogenesis. Cell Rep 33, 108394. 10.1016/j.celrep.2020.108394. [PubMed: 33207207]
57. Baxi EG, DeBruin J, Jin J, Strasburger HJ, Smith MD, Orthmann-Murphy JL, Schott JT, Fairchild AN, Bergles DE, and Calabresi PA (2017). Lineage tracing reveals dynamic changes in oligodendrocyte precursor cells following cuprizone-induced demyelination. Glia 65, 2087–2098. 10.1002/glia.23229. [PubMed: 28940645]
58. Yang Y, Wang H, Zhang J, Luo F, Herrup K, Bibb JA, Lu R, and Miller RH (2013). Cyclin dependent kinase 5 is required for the normal development of oligodendrocytes and myelin formation. Dev. Biol 378, 94–106. 10.1016/j.ydbio.2013.03.023. [PubMed: 23583582]
59. Hirasawa M, Ohshima T, Takahashi S, Longenecker G, Honjo Y, Veeranna, null, Pant HC, Mikoshiba K, Brady RO, and Kulkarni AB (2004). Perinatal abrogation of Cdk5 expression in brain results in neuronal migration defects. Proc. Natl. Acad. Sci. U. S. A 101, 6249–6254. 10.1073/pnas.0307322101. [PubMed: 15067135]
60. Moyon S, Dubessy AL, Aigrot MS, Trotter M, Huang JK, Dauphinot L, Potier MC, Kerninon C, Parsadaniantz SM, Franklin RJM, et al. (2015). Demyelination Causes Adult CNS Progenitors to

Revert to an Immature State and Express Immune Cues That Support Their Migration. J. Neurosci 35, 4–20. 10.1523/JNEUROSCI.0849-14.2015. [PubMed: 25568099]

61. Golalipour M, Maleki Z, Farazmandfar T, and Shahbazi M (2017). PER3 VNTR polymorphism in Multiple Sclerosis: A new insight to impact of sleep disturbances in MS. Mult. Scler. Relat. Disord 17, 84–86. 10.1016/j.msard.2017.07.005. [PubMed: 29055480]
62. Toschi N, Passamonti L, and Bellesi M (2021). Sleep quality relates to emotional reactivity via intracortical myelination. Sleep 44, zsaa146. 10.1093/sleep/zsaa146. [PubMed: 32770244]
63. Auguste YSS, Ferro A, Kahng JA, Xavier AM, Dixon JR, Vrudhula U, Nichitiu A-S, Rosado D, Wee T-L, Pedmale UV, et al. (2022). Oligodendrocyte precursor cells engulf synapses during circuit remodeling in mice. Nat. Neurosci 25, 1273–1278. 10.1038/s41593-022-01170-x. [PubMed: 36171430]
64. Bellesi M, Haswell JD, de Vivo L, Marshall W, Roseboom PH, Tononi G, and Cirelli C (2018). Myelin modifications after chronic sleep loss in adolescent mice. Sleep 41. 10.1093/sleep/zsy034.
65. Chen P, Ban W, Wang W, You Y, and Yang Z (2023). The Devastating Effects of Sleep Deprivation on Memory: Lessons from Rodent Models. Clocks Sleep 5, 276–294. 10.3390/clockssleep5020022. [PubMed: 37218868]
66. Li P, Gao L, Yu L, Zheng X, Ulsa MC, Yang H-W, Gaba A, Yaffe K, Bennett DA, Buchman AS, et al. (2022). Daytime napping and Alzheimer’s dementia: A potential bidirectional relationship. Alzheimers Dement. J. Alzheimers Assoc 10.1002/alz.12636.
67. Mander BA, Winer JR, Jagust WJ, and Walker MP (2016). Sleep: A Novel Mechanistic Pathway, Biomarker, and Treatment Target in the Pathology of Alzheimer’s Disease? Trends Neurosci 39, 552–566. 10.1016/j.tins.2016.05.002. [PubMed: 27325209]
68. Emery B, and Dugas JC (2013). Purification of oligodendrocyte lineage cells from mouse cortices by immunopanning. Cold Spring Harb. Protoc 2013, 854–868. 10.1101/pdb.prot073973. [PubMed: 24003195]
69. Zuchero JB, Fu M, Sloan SA, Ibrahim A, Olson A, Zaremba A, Dugas JC, Wienbar S, Caprariello AV, Kantor C, et al. (2015). CNS Myelin Wrapping Is Driven by Actin Disassembly. Dev. Cell 34, 152–167. 10.1016/j.devcel.2015.06.011. [PubMed: 26166300]
70. Love MI, Huber W, and Anders S (2014). Moderated estimation of fold change and dispersion for RNA-seq data with DESeq2. Genome Biol 15, 550. 10.1186/s13059-014-0550-8. [PubMed: 25516281]
71. Benjamini Y, and Hochberg Y (1995). Controlling the False Discovery Rate: A Practical and Powerful Approach to Multiple Testing. J. R. Stat. Soc. Ser. B Methodol 57, 289–300. 10.1111/j.25176161.1995.tb02031.x.
72. Hughes ME, Hogenesch JB, and Kornacker K (2010). JTK_CYCLE: an efficient non-parametric algorithm for detecting rhythmic components in genome-scale datasets. J. Biol. Rhythms 25, 372–380. 10.1177/0748730410379711. [PubMed: 20876817]
73. Brooks TG, Mrčela A, Lahens NF, Paschos GK, Grosser T, Skarke C, FitzGerald GA, and Grant GR (2022). Nitecap: An Exploratory Circadian Analysis Web Application. J. Biol. Rhythms 37, 43–52. 10.1177/07487304211054408. [PubMed: 34724846]
74. Sudlow C, Gallacher J, Allen N, Beral V, Burton P, Danesh J, Downey P, Elliott P, Green J, Landray M, et al. (2015). UK biobank: an open access resource for identifying the causes of a wide range of complex diseases of middle and old age. PLoS Med 12, e1001779. 10.1371/journal.pmed.1001779. [PubMed: 25826379]
75. Zöllner S, and Pritchard JK (2007). Overcoming the Winner’s Curse: Estimating Penetrance Parameters from Case-Control Data. Am. J. Hum. Genet 80, 605–615. 10.1086/512821. [PubMed: 17357068]
76. Bowden J, and Dudbridge F (2009). Unbiased estimation of odds ratios: combining genomewide association scans with replication studies. Genet. Epidemiol 33, 406–418. 10.1002/gepi.20394. [PubMed: 19140132]
77. Palmer C, and Pe’er I (2017). Statistical correction of the Winner’s Curse explains replication variability in quantitative trait genome-wide association studies. PLOS Genet 13, e1006916. 10.1371/journal.pgen.1006916. [PubMed: 28715421]

78. Taylor AE, Davies NM, Ware JJ, VanderWeele T, Smith GD, and Munafò MR (2014). Mendelian randomization in health research: Using appropriate genetic variants and avoiding biased estimates. Econ. Hum. Biol 13, 99–106. 10.1016/j.ehb.2013.12.002. [PubMed: 24388127]

79. Burgess S, Butterworth A, and Thompson SG (2013). Mendelian Randomization Analysis With Multiple Genetic Variants Using Summarized Data. Genet. Epidemiol 37, 658–665. 10.1002/gepi.21758. [PubMed: 24114802]

80. Bowden J, Davey Smith G, Haycock PC, and Burgess S (2016). Consistent Estimation in Mendelian Randomization with Some Invalid Instruments Using a Weighted Median Estimator. Genet. Epidemiol 40, 304–314. 10.1002/gepi.21965. [PubMed: 27061298]

81. Burgess S, and Thompson SG (2017). Interpreting findings from Mendelian randomization using the MREgger method. Eur. J. Epidemiol 32, 377–389. 10.1007/s10654-017-0255-x. [PubMed: 28527048]

82. Brion M-JA, Shakhbazov K, and Visscher PM (2013). Calculating statistical power in Mendelian randomization studies. Int. J. Epidemiol 42, 1497–1501. 10.1093/ije/dyt179. [PubMed: 24159078]

Highlights:

1. BMAL1 regulates genes that control OPC proliferation, migration and morphology.
2. Knock out of BMAL1 in OPCs dysregulates these oligodendroglial dynamics.
3. Knock out of BMAL1 in OPCs leads to deficits in myelination and remyelination.
4. The cellular and myelin deficits lead to neurological and sleep dysfunction.

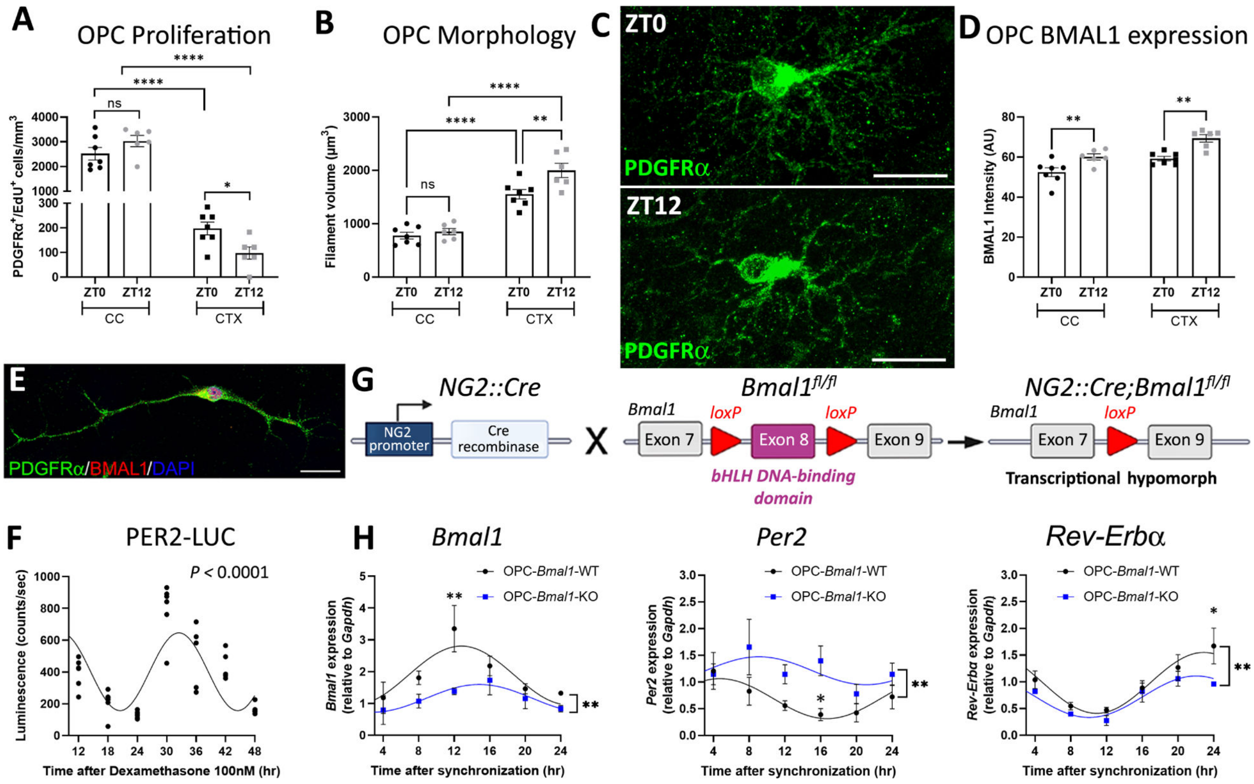

Figure 1. Time-of-day differences in OPC physiology and circadian gene oscillations.

(A-D) WT OPC dynamics throughout the circadian day. **(A)** EdU was injected in a single pulse 30 min before perfusion of P21 WT mice. OPC proliferation is significantly higher at the zeitgeber time (ZT) 0 than ZT12 assessed by EdU$^+$/PDGFRα$^+$ co-labelling in the grey matter (cortex, CTX) (ZT0, $n = 7$; ZT12, $n = 6$; $*P = 0.0287$) but not in the white matter (corpus callosum, CC) (ZT0, $n = 7$; ZT12, $n = 6$; $P = 0.2819$). **(B)** Morphological complexity (filament volume) of OPCs is significantly higher at ZT12 than ZT0 in the cortex (ZT0, $n = 7$; ZT12, $n = 6$; $**P = 0.0039$) but not in corpus callosum (ZT0, $n = 7$; ZT12, $n = 6$; $P = 0.5648$). **(C)** Photomicrograph (63X) of PDGFRα$^+$ OPCs (green) in the cortex at ZT0 (top) and ZT12 (bottom); Scale bar = 20 μm. **(D)** BMAL1 immunofluorescence intensity is significantly higher at ZT12 than ZT0 in the corpus callosum (ZT0, $n = 7$; ZT12, $n = 6$; $**P = 0.0087$) and cortex (ZT0, $n = 7$; ZT12, $n = 6$; $**P = 0.0027$). **(E)** Photomicrograph (63X) of PDGFRα$^+$ OPCs (green) expressing BMAL1 (red) with DAPI (blue) in immunopan-isolated OPCs from P6 mice; Scale bar = 20 μm. **(F)** Luciferase activity in isolated OPCs from P6 PER2::LUCIFERASE mice that express a fusion protein of PER2 and LUCIFERASE. Treating OPCs with 100 mM dexamethasone for 1 hr synchronizes the circadian molecular clocks of OPCs *in vitro* ($n = 5$–6; $P<0.0001$ One-way ANOVA for CT, $P<0.0001$ JTK Cycle). **(G)** The conditional *Bmal1* knock out model *Bmal1*$^{fl/fl}$, in which the eighth exon coding for the basic helix-loop-helix DNA-binding domain is surrounded by loxP sites, was bred to the OPC-specific *Cre* driver mouse model *NG2::Cre* to create a *Bmal1* transcriptional hypomorph mouse model in which only the DNA-binding domain of BMAL1 is eliminated specifically in OPCs (*NG2::Cre+;Bmal1*$^{fl/fl}$ or OPC-*Bmal1*-KO), thus creating a functional knock out model. **(H)** *Bmal1* (OPC-*Bmal1*-WT, $n = 3$; OPC-*Bmal1*-

KO, *n* = 4; ***P* = 0.0013 Two-way ANOVA genotype; ***P = 0.0026 CT12*), *Per2* (*n* = 4; ***P* = 0.0011 Two-way ANOVA genotype; **P = 0.0493 CT16*), and *Rev-Erbα* expression (*n* = 4; ***P* = 0.0062 Two-way ANOVA genotype; **P = 0.0139 CT24*) measured by RT-qPCR relative to *Gapdh* across 24 hr circadian time (CT) in OPCs with (OPC-*Bmal1*-WT) or without (OPC-*Bmal1*-KO) functional *Bmal1*. Data shown as mean +/− S.E.M. n.s. P >0.05.

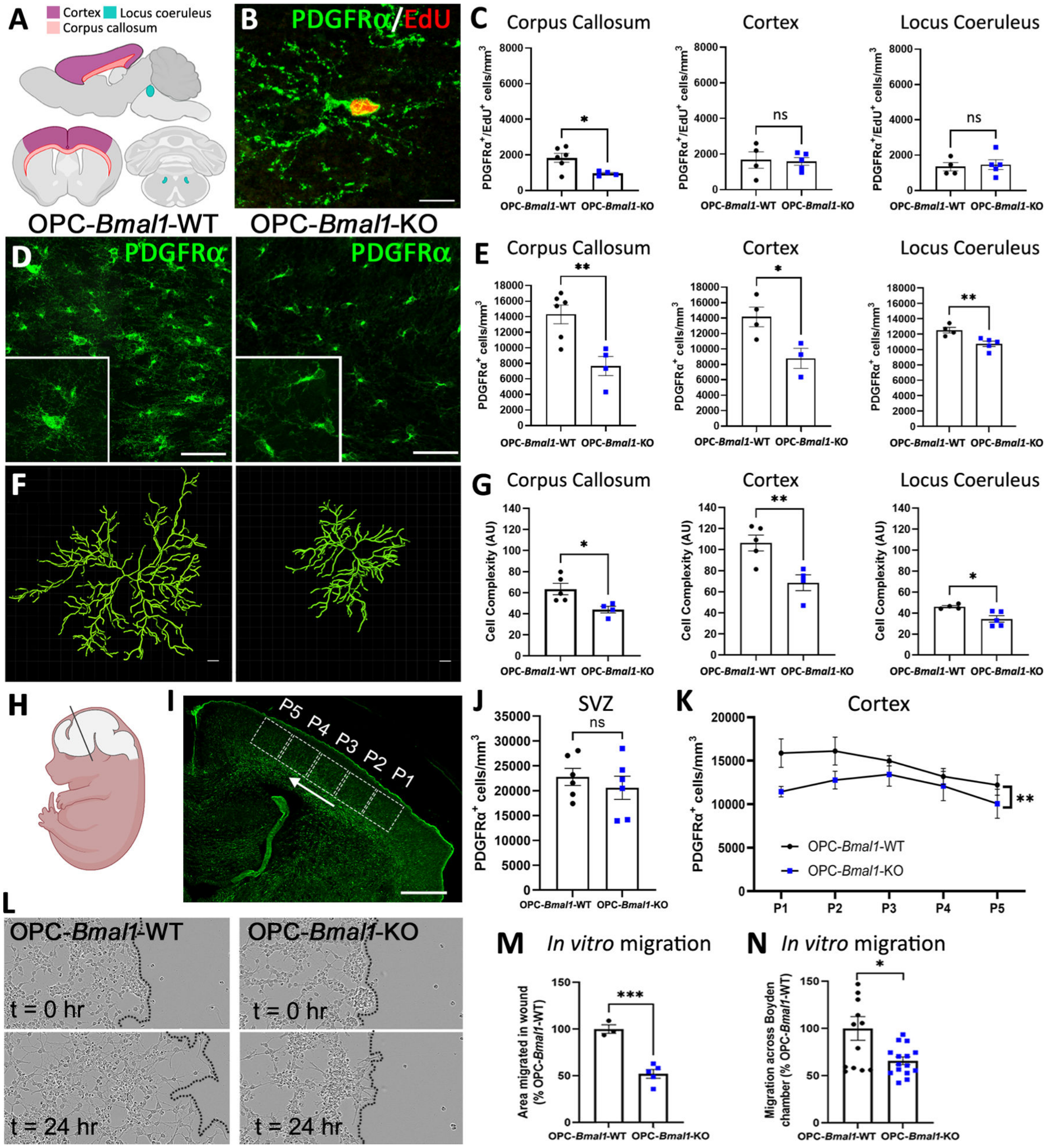

Figure 2. Functional knock out of *Bmal1* in OPCs during embryonic development affects oligodendroglial lineage dynamics.

(A) Schematic of the brain regions assessed in P21 mice, showing the corpus callosum (pink), the cortex (purple), and locus coeruleus (teal). **(B)** Photomicrograph (63X) of PDGFRα$^+$ (green) OPC with EdU (red). Scale bar = 10 μm. **(C)** The functional loss of *Bmal1* from OPCs results in a 48% decrease in OPC proliferation assessed by EdU$^+$/PDGFRα$^+$ co-labelling in the corpus callosum (OPC-*Bmal1*-WT, *n* = 6; OPC-*Bmal1*-KO, *n* = 4; **P* = 0.0252) but not in cortex or locus coeruleus. **(D)** Photomicrographs (20X; inset 63X) of PDGFRα$^+$ (green) OPCs in the corpus callosum of OPC-*Bmal1*-WT (left) and OPC-*Bmal1*-KO (right) mice. Scale bar = 50 μm. **(E)** OPC-*Bmal1*-KO mice exhibit a significant decrease in PDGFRα$^+$ OPC density compared to OPC-*Bmal1*-WT OPCs in the corpus callosum (OPC-*Bmal1*-WT, $n = 6$; OPC-*Bmal1*-KO, $n = 4$; $^{**}P = 0.0061$), cortex (OPC-*Bmal1*-WT, $n = 4$; OPC-*Bmal1*-KO, $n = 3$; $^{*}P = 0.0332$) and locus coeruleus (OPC-*Bmal1*-WT, $n = 4$; OPC-*Bmal1*-KO, $n = 5$; $^{**}P = 0.01$). **(F)** Representative tracings of OPC morphological complexity using Imaris in OPC-*Bmal1*-WT (left) and OPC-*Bmal1*-KO (right). Scale bar = 5 μm. **(G)** Morphological complexity (ratio of branch points and filament length by filament volume) of OPCs in the corpus callosum (OPC-*Bmal1*-WT, $n = 5$; OPC-*Bmal1*-KO, $n = 4$; $^{*}P = 0.0232$), cortex (OPC-*Bmal1*-WT, $n = 5$; OPC-*Bmal1*-KO, $n = 4$; $^{**}P = 0.01$), and locus coeruleus (OPC-*Bmal1*-WT, $n = 4$; OPC-*Bmal1*-KO, $n = 5$; $^{*}P = 0.0148$). **(H-K)** OPC establishment from the subventricular germinal zone (SVZ) during development is reduced in *NG2::Cre+;Bmal1*$^{fl/fl}$ (OPC-*Bmal1*-KO) mice. **(H)** Schematic of the brain region analyzed in P0 mice. **(I)** Photomicrograph (10X) of PDGFRα^{+} (green) OPCs at P0 showing a representative image of OPC densities analyzed across 5 positions (P1–5) in the cortex. Scale bar = 500 μm. **(J-K)** PDGFRα^{+} OPC density is not affected in the SVZ ($n = 6$; $P = 0.4701$) **(J)** but is reduced across the cortex compared to controls **(K)**. **(K)** OPC densities were determined across the cortex of each mouse (OPC-*Bmal1*-WT, $n = 5$; OPC-*Bmal1*-KO, $n = 6$; $^{**}P = 0.0041$ Two-way ANOVA Genotype). **(L-N)** OPCs isolated from OPC-*Bmal1*-KO P6 mice exhibit a delay in migration *in vitro*. **(L)** Photomicrographs (10X) of OPC-*Bmal1*-WT (left) and OPC-*Bmal1*-KO (right) OPCs at time 0 hr (top) and 24 hr (bottom) of the wound. **(M)** Relative wound closure was determined by measuring the area covered by OPCs at time 0 and after 24 hr (OPC-*Bmal1*-WT, $n = 3$; OPC-*Bmal1*-KO, $n = 5$; $^{***}P = 0.0005$). **(N)** Relative migration through 8μm-pore Boyden chambers after 24 hr incubation determined through crystal violet staining (OPC-*Bmal1*-WT, $n = 13$; OPC-*Bmal1*-KO, $n = 15$ over 3 independent experiments; $^{*}P = 0.0104$). Data shown as mean +/− S.E.M. n.s. P >0.05.

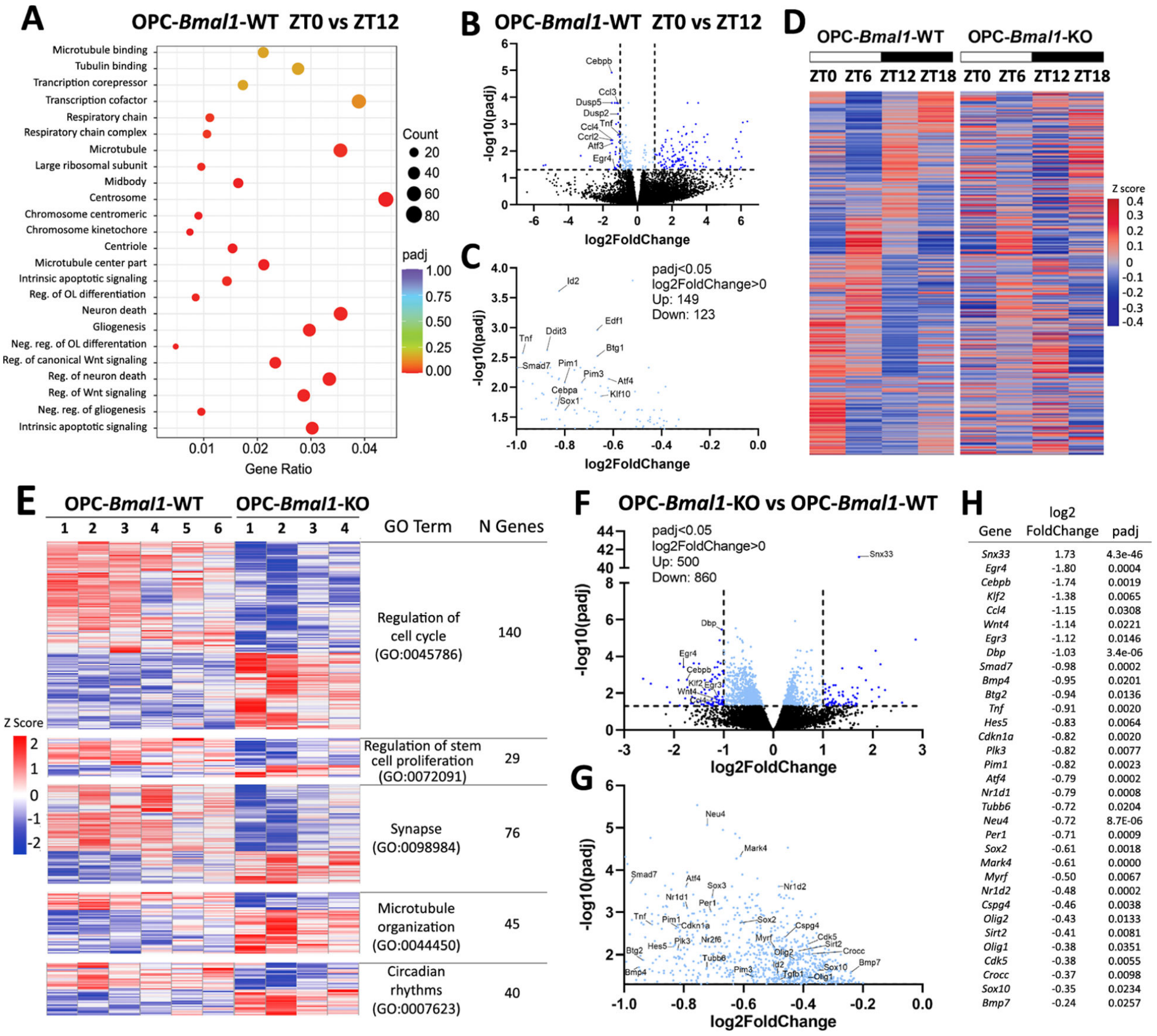

Gene	log2 FoldChange	padj
Snx33	1.73	4.3e-46
Egr4	-1.80	0.0004
Cebpb	-1.74	0.0019
Klf2	-1.38	0.0065
Ccl4	-1.15	0.0308
Wnt4	-1.14	0.0221
Egr3	-1.12	0.0146
Dbp	-1.03	3.4e-06
Smad7	-0.98	0.0002
Bmp4	-0.95	0.0201
Btg2	-0.94	0.0136
Tnf	-0.91	0.0020
Hes5	-0.83	0.0064
Cdkn1a	-0.82	0.0020
Plk3	-0.82	0.0077
Pim1	-0.82	0.0023
Atf4	-0.79	0.0002
Nr1d1	-0.79	0.0008
Tubb6	-0.72	0.0204
Neu4	-0.72	8.7E-06
Per1	-0.71	0.0009
Sox2	-0.61	0.0018
Mark4	-0.61	0.0000
Myrf	-0.50	0.0067
Nr1d2	-0.48	0.0002
Cspg4	-0.46	0.0038
Olig2	-0.43	0.0133
Sirt2	-0.41	0.0081
Olig1	-0.38	0.0351
Cdk5	-0.38	0.0055
Crocc	-0.37	0.0098
Sox10	-0.35	0.0234
Bmp7	-0.24	0.0257

Figure 3. BMAL1 regulates the expression of genes that contribute to the homeostatic dynamics of OPCs.

Bulk RNA sequencing was performed in immuno-pan isolated OPCs from P6–7 OPC-*Bmal1*-WT and OPC-*Bmal1*-KO mice at 6-h intervals for 24 h (OPC-*Bmal1*-WT: ZT0 *n* = 4, ZT6 *n* = 5, ZT12 *n* = 6, ZT18 *n* = 4; OPC-*Bmal1*-KO: ZT0 *n* = 4, ZT6 *n* = 7, ZT12 *n* = 4, ZT18 *n* = 4). **(A-E)** Genes identified to be specifically rhythmic in BMAL1-intact OPCs are enriched in modulators of cell cycle, apoptosis, oligodendrocyte differentiation, gliogenesis, and microtubule binding. **(A)** Gene Ontology (GO) pathways enriched in differentially expressed genes in BMAL1-intact OPCs between ZT0 and ZT12. **(B-C)** Volcano plot showing differential gene expression in RNA-seq from OPC-*Bmal1*-WT at ZT0 compared to ZT12 **(B)** and inset **(C)**. Genes with adjusted p value < 0.05 and $\log_2$ fold change > 1 are shown in dark blue, and genes with adjusted p value < 0.05 and $\log_2$ fold change < 1 are shown in light blue. **(D)** JTK Cycle analysis using FPKMs as inputs shows that the rhythmicity of gene expression in OPCs from OPC-*Bmal1*-WT mice (left) changes in OPCs that lack a functional BMAL1 (right). The heatmap represents all normalized counts combined per genotype and ZT and clustered by time of peak expression in OPC-*Bmal1*-WT OPCs. **(E)** Heatmaps of genes clustered based on gene expression differences between OPC-*Bmal1*-WT and OPC-*Bmal1*-KO OPCs at ZT12, organized by top GO terms. **(F-G)** Volcano plot showing that OPCs from OPC-*Bmal1*-KO mice have a downregulation of 860 genes compared to OPCs from OPC-*Bmal1*-WT mice at ZT12 **(F)**, inset **(G)**, and corresponding table showing the Log2FoldChange and p adjusted values of the genes marked in the volcano plot **(H)**.

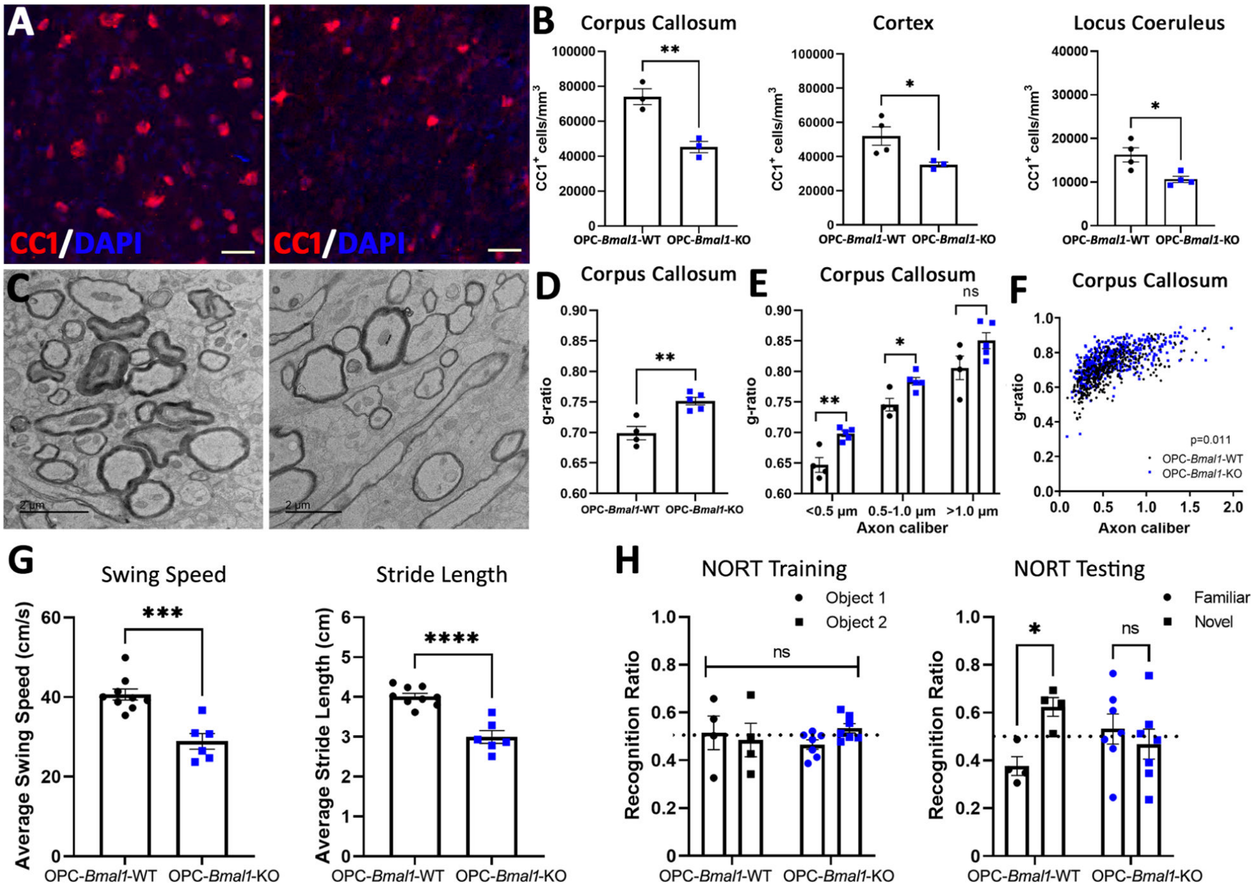

Figure 4. BMAL1 functional knock out in OPCs dysregulates oligodendrocytes, myelination, motor, and cognitive function.

(A) Photomicrographs (20X) of CC1$^+$ (red) oligodendrocytes with DAPI (blue) in the corpus callosum at P21. Scale bar = 30 μm. (B) OPC-*Bmal1*-KO have decreased CC1$^+$ oligodendrocyte density in the corpus callosum (*n* = 3; ***P* = 0.0067), cortex (OPC-*Bmal1*-WT, *n* = 4; OPC-*Bmal1*-KO, *n* = 3; **P* = 0.0493) and locus coeruleus (*n* = 4; **P* = 0.0193) at P21 compared to OPC-*Bmal1*-WT mice. (C) Representative TEM images of the corpus callosum at the level of the cingulum in OPC-*Bmal1*-WT (left) and OPC-*Bmal1*-KO (right) mice at P21. Scale bar = 2 μm. (D) g-ratio of axons in the corpus callosum of OPC-*Bmal1*-WT and OPC-*Bmal1*-KO mice at P21 (larger g-ratio = thinner myelin) (OPC-*Bmal1*-WT, *n* = 4; OPC-*Bmal1*-KO, *n* = 5; ***P* = 0.0033) and (E) g-ratio by axon caliber (OPC-*Bmal1*-WT, *n* = 4; OPC-*Bmal1*-KO, *n* = 5; <0.5μm ***P* = 0.0034; 0.5–1μm **P* = 0.0123; >1μm; *P* = 0.0874). (F) Scatterplot of *g*-ratios as a function of axon caliber of all axons measured. Each point represents a single axon (100 axons per mouse; OPC-*Bmal1*-WT, *n* = 4; OPC-*Bmal1*-KO, *n* = 5; **P* = 0.011). (G) OPC-*Bmal1*-KO exhibit deficits in swing speed of limbs and shorter stride length at P35 assessed using the CatWalk gait analysis system compared to OPC-*Bmal1*-WT mice (OPC-*Bmal1*-WT, *n* = 9; OPC-*Bmal1*-KO, *n* = 6; speed: ****P* = 0.0003; length: *****P* <0.0001). (H) OPC-*Bmal1*-KO mice exhibit attention and short-term memory deficits at 7 months assessed using a modified novel object recognition test (NORT) in which the interval between training and testing is shortened to 5 minutes. OPC-*Bmal1*-KO mice do not discriminate between the novel and familiar objects whereas

OPC-*Bmal1*-WT spend more time investigating the novel over familiar object OPC-*Bmal1*-WT, $n = 4$; OPC-*Bmal1*-KO, $n = 7$; $P = 0.0244$ for Two-way ANOVA interaction, *$P = 0.0489$ for OPC-*Bmal1*-WT, $P = 0.4155$ for OPC-*Bmal1*-KO). Data shown as mean +/− S.E.M. n.s. $P > 0.05$.

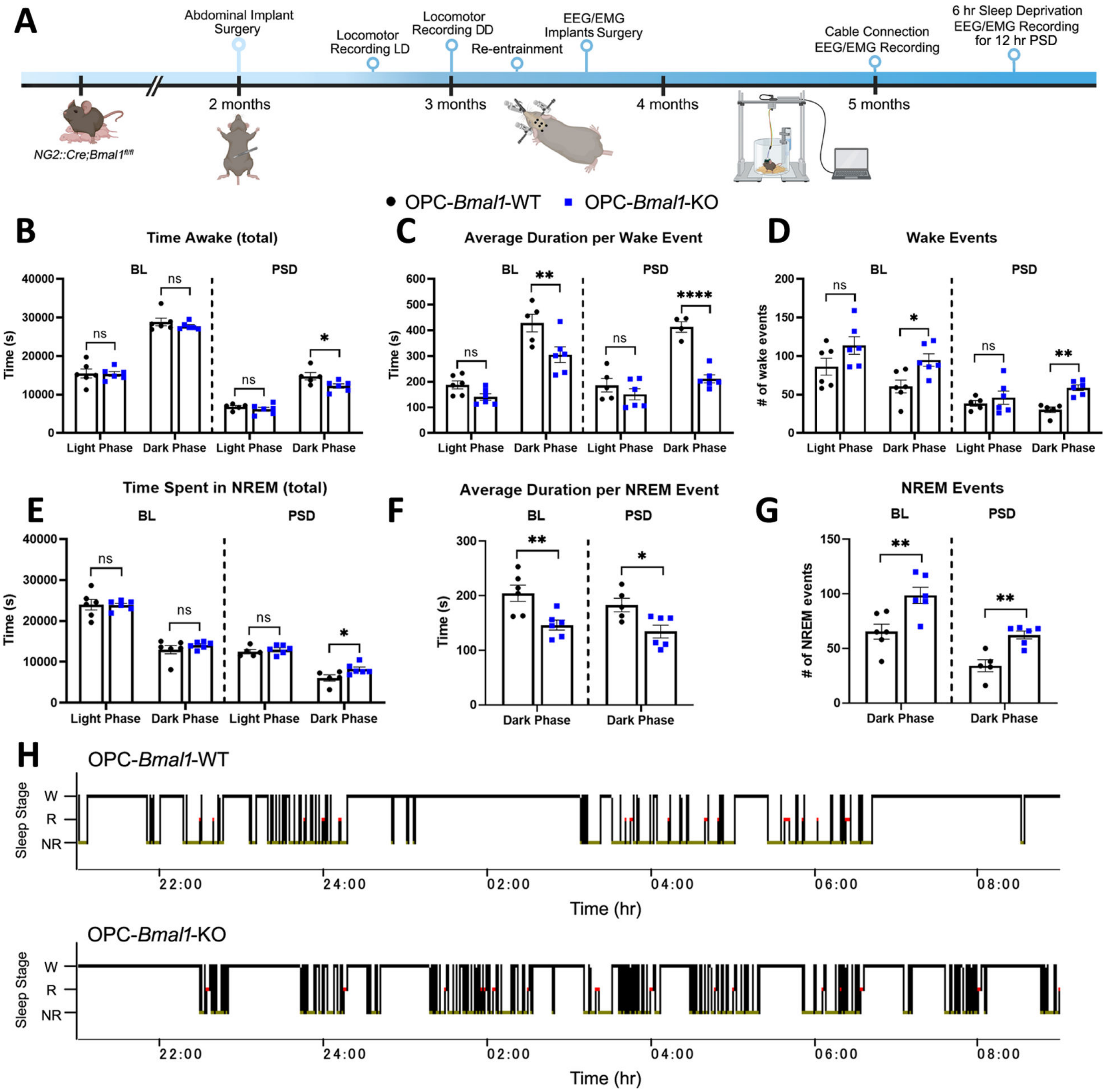

Figure 5. Functional loss of *Bmal1* specifically in OPCs is associated with abnormal sleep architecture in mice.

(A) At 2 months of age, OPC-*Bmal1*-WT and OPC-*Bmal1*-KO mice were subjected to abdominal surgery to implant electronic transmitters. Locomotor activity was telemetrically monitored in light/dark (LD) cycles for 7 days followed by constant darkness (DD) for 15 days. EMG/EEG biotelemetry electrodes were then implanted at 3.5 months and baseline (BL) sleep was recorded at 5 months for 10 days. Mice were then subjected to a 6-hr sleep deprivation (SD) cycle and sleep waves were recorded for 12 hrs post sleep deprivation (PSD). **(B-D)** While OPC-*Bmal1*-WT and OPC-*Bmal1*-KO mice spend the same total amount of time awake and asleep during both the light/sleep and dark/active phase at baseline ($n = 6$) **(B left)**, OPC-*Bmal1*-KO mice have shorter (OPC-*Bmal1*-WT, $n = 5$; OPC-*Bmal1*-KO, $n = 6$; $^{**}P = 0.0046$) **(C left)**, more frequent wake bouts ($n = 6$; $^{*}P$

= 0.0434) **(D left)** during the dark phase than OPC-*Bmal1*-WT mice, indicative of sleep fragmentation. Post-sleep deprivation (PSD), OPC-*Bmal1*-KO mice exhibit a significant decrease in the amount of wake during their dark/active phase compared to OPC-*Bmal1*-WT mice (**B right**; OPC-*Bmal1*-WT, *n* = 5; OPC-*Bmal1*-KO, *n* = 6; **P* = 0.0199). This increased active-phase sleep following sleep deprivation exhibits the same pattern of sleep fragmentation as detected during baseline as they have shorter (**C right**; OPC-*Bmal1*-WT, *n* = 4; OPC-*Bmal1*-KO, *n* = 6; *****P* <0.0001) but more frequent wake bouts (**D right**; OPC-*Bmal1*-WT, *n* = 5; OPC-*Bmal1*-KO, *n* = 6; ***P*=0.0043). **(E-G)** The shift in sleep architecture at BL is driven by changes in NREM sleep, as total amount of NREM does not differ between the genotypes (*n* = 6; *P* = 0.631) **(E left)**, but OPC-*Bmal1*-KO mice exhibit the same trend of shorter (*n* = 6; ***P*=0.0076) **(F left)** but more frequent (*n* = 6; ***P*=0.0083) **(G left)** NREM events during the dark/active phase. Post-sleep deprivation, OPC-*Bmal1*-KO spend more time in NREM sleep compared to OPC-*Bmal1*-WT mice (OPC-*Bmal1*-WT, *n* = 5; OPC-*Bmal1*-KO, *n* = 6; **P*=0.0314) **(E right)**, which is driven by shorter (OPC-*Bmal1*-WT, *n* = 5; OPC-*Bmal1*-KO, *n* = 6; **P*=0.0191) **(F right)**, more frequent (OPC-*Bmal1*-WT, *n* = 5; OPC-*Bmal1*-KO, *n* = 6; ***P*=0.0016) **(G right)** bouts. **(H)** Representative hypnograms showing wake (W), REM (R) and NREM (NR) sleep events during the dark phase (21:00 hr – 9:00 hr) at BL in OPC-*Bmal1*-WT (top) and OPC-*Bmal1*-KO (bottom) mice. Data shown as mean +/− S.E.M. n.s. P>0.05.

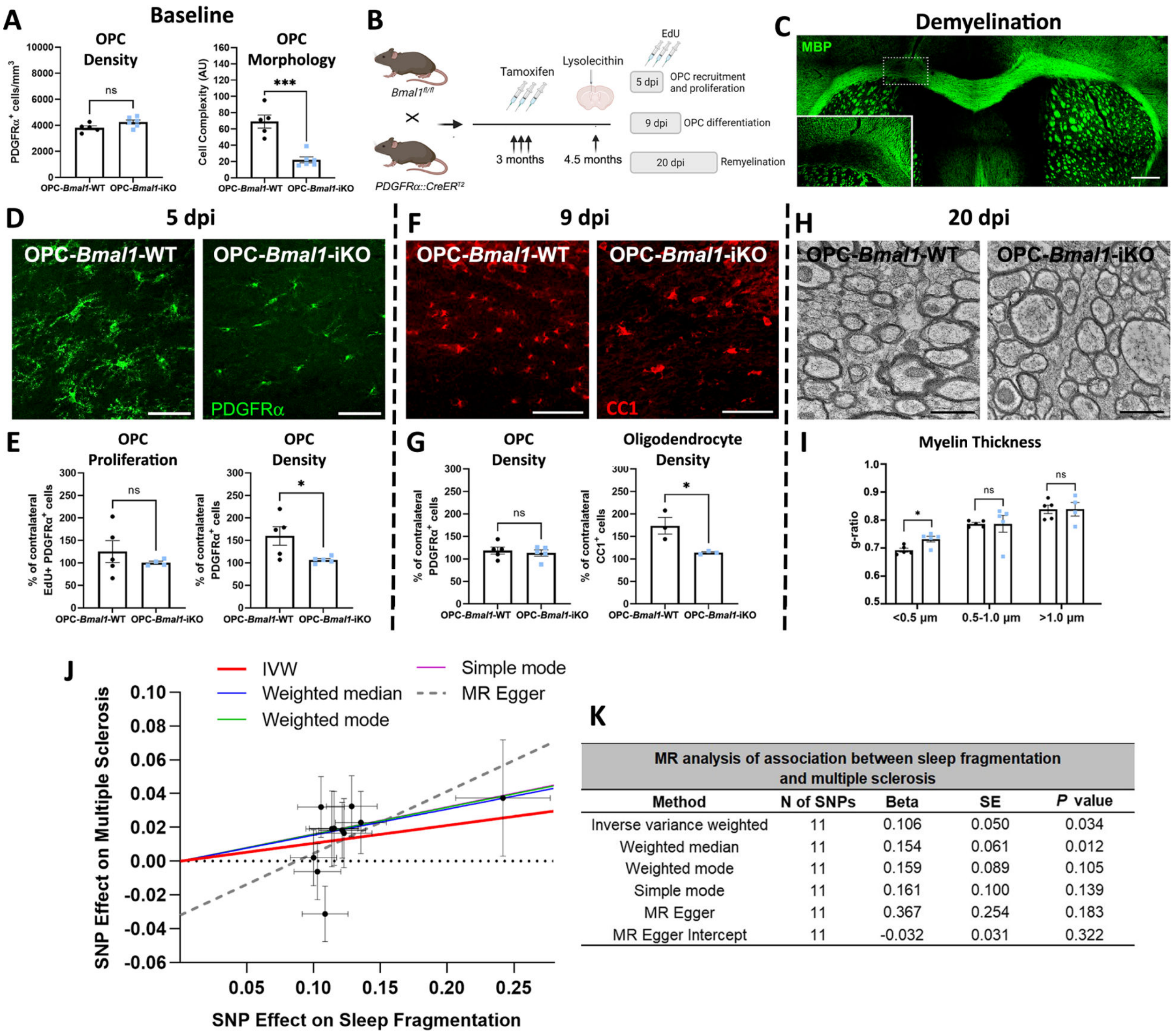

MR analysis of association between sleep fragmentation and multiple sclerosis				
Method	N of SNPs	Beta	SE	*P* value
Inverse variance weighted	11	0.106	0.050	0.034
Weighted median	11	0.154	0.061	0.012
Weighted mode	11	0.159	0.089	0.105
Simple mode	11	0.161	0.100	0.139
MR Egger	11	0.367	0.254	0.183
MR Egger Intercept	11	-0.032	0.031	0.322

Figure 6. Impaired remyelination potential is associated with sleep fragmentation in both mice and humans.

(A) Tamoxifen-induced functional knock out of *Bmal1* in OPCs (*PDGFRα::CreER*^{T2}*+;Bmal1*$^{fl/fl}$ or OPC-*Bmal1*-iKO) at 3 months of age leads to decreased complexity in OPC morphology (OPC-*Bmal1*-WT, *n* = 5, OPC-*Bmal1*-iKO, *n* = 6, ****P* = 0.0003) without disrupting OPC density (OPC-*Bmal1*-WT, *n* = 5, OPC-*Bmal1*-iKO, *n* = 6, *P* = 0.0787). **(B-C)** Six weeks after tamoxifen-induced Cre recombination, OPC-*Bmal1*-iKO and their control littermates (*PDGFRα::CreER*^{T2}*−;Bmal1*$^{fl/fl}$ or OPC-*Bmal1*-WT) were injected with lysolecithin into the cingulum of the corpus callosum of one hemisphere and brains were collected after 5, 9 or 20 days post-injection (dpi). Cellular densities were compared to the contralateral non-lesioned hemisphere. **(C)** Photomicrograph (10X) of MBP (green) showing the demyelinating lesion in the cingulum of the corpus callosum. Scale bar = 500 µm. **(D)** Photomicrographs (20X) of PDGFRα$^+$ (green) OPCs in the corpus callosum at 5 dpi. Scale bar = 50 µm. **(E)** 5 days after demyelination, OPC density in the lesion compared to the contralateral non-lesioned hemisphere is decreased in OPC-

Bmal1-iKO compared to OPC-*Bmal1*-WT mice (*n* = 5; **P* = 0.0335), which is unrelated to OPC proliferation (OPC-*Bmal1*-WT, *n* = 5; OPC-*Bmal1*-iKO, *n* = 4; *P* = 0.4037). **(F)** Photomicrographs (20X) of CC1$^+$ (red) oligodendrocytes in the corpus callosum at 9 dpi. Scale bar = 50µm. **(G)** 9 days after lysolecithin-induced demyelination, oligodendrocyte density in the lesion is significantly lower in OPC-*Bmal1*-iKO compared to OPC-*Bmal1*-WT mice (*n* = 3; **P* = 0.0322), with no differences in OPC density (*n* = 5, *P* = 0.6125). **(H)** Representative TEM images of the corpus callosum in OPC-*Bmal1*-WT (left) and OPC-*Bmal1*-iKO (right) mice at 20 dpi. Scale bar = 1 µm. **(I)** At 20 dpi, myelin sheath thickness is decreased in small caliber axons of OPC-*Bmal1*-iKO compared to OPC-*Bmal1*-WT mice (*n* = 5; **P* = 0.0118). Data shown as mean +/−SEM. n.s. P>0.05. **(J)** Scatterplot of the mendelian randomization (MR) analysis of association between sleep fragmentation and multiple sclerosis (MS). MR analyses were performed on lead variants identified in a GWAS of sleep fragmentation (defined as number of sleep episodes) in 85,723 UK Biobank individuals. By using genetic proxies for the exposure (sleep fragmentation) and assessing how they influence the outcome (risk of MS), we estimate the true effect of the exposure on the outcome and not the effect that comes from the genetics only. The y-axis represents the effect of the analyzed variants on MS (beta) and the x-axis represents the variants effect on the number of sleep episodes (logOddsRatio) for each of the 11 variants studied. The slopes of the regression lines represent the association tested using Inverse variance weighted (IVW), Weighted median, Weighted mode, Simple mode, and MR Egger statistical tests. **(K)** Corresponding table of the MR analysis performed indicates causal association between sleep fragmentation and MS risk without pleiotropic effect (MR Egger Intercept *P* = 0.32). Beta, β coefficient; SE, Standard Error.

KEY RESOURCES TABLE

REAGENT or RESOURCE	SOURCE	IDENTIFIER
Antibodies		
Goat polyclonal anti-PDGFRα	R&D Systems	Cat# AF1062; RRID: AB_2236897
Mouse monoclonal anti-CC1	Millipore	Cat# OP80; RRID: AB_2057371
Rabbit polyclonal anti-BMAL1	Novus Biologicals	Cat# NB100–2288; RRID: AB_10000794
Chicken polyclonal anti-Tyrosine Hydroxylase (TH)	Aves lab	Cat# TYH; RRID: AB_10013440
Goat polyclonal anti-CD31/PECAM1	R&D Systems	Cat# AF3628; RRID: AB_2161028
Rat monoclonal anti-CD13	Biorad	Cat# MCA2183; RRID: AB_323691
Rat monoclonal anti-myelin basic protein (MBP)	Abcam	Cat# ab7349; RRID: AB_305869
Rat monoclonal anti-CD140A	BD Pharmingen	Cat# 558774; RRID: AB_397117
Rabbit polyclonal anti-NG2 Chondroitin Sulfate Proteoglycan	Millipore	Cat# AB5320; RRID: AB_11213678
Rat monoclonal anti-GAPDH	BioLegend	Cat# 607903; RRID: AB_2734504
Alexa 488 sheep anti-mouse IgG	Jackson Immunoresearch	Cat# 515-545-072; RRID: AB_2340335
Alexa 594 donkey anti-mouse IgG	Jackson Immunoresearch	Cat# 715-585-150; RRID: AB_2340854
Alexa 647 donkey anti-mouse IgG	Jackson Immunoresearch	Cat# 715-605-150; RRID: AB_2340862
Alexa 488 donkey anti-rabbit IgG	Jackson Immunoresearch	Cat# 711-546-152; RRID: AB_2340619
Alexa 594 donkey anti-rabbit IgG	Jackson Immunoresearch	Cat# 711-586-152; RRID: AB_2340622
Alexa 647 donkey anti-rabbit IgG	Jackson Immunoresearch	Cat# 711-605-152; RRID: AB_2492288
Alexa 488 donkey anti-goat IgG	Jackson Immunoresearch	Cat# 705-545-147; RRID: AB_2336933
Alexa 594 donkey anti-goat IgG	Jackson Immunoresearch	Cat# 705-586-147; RRID: AB_2340434
Alexa 647 donkey anti-goat IgG	Jackson Immunoresearch	Cat# 705-606-147; RRID: AB_2340438
Alexa 488 donkey anti-rat IgG	Jackson Immunoresearch	Cat# 712-545-153; RRID: AB_2340684
Alexa 594 goat anti-rat IgG	Jackson Immunoresearch	Cat# 112-005-167; RRID: AB_2338101
Alexa 647 donkey anti-rat IgG	Jackson Immunoresearch	Cat# 712-586-150; RRID: AB_2340690
Bacterial and virus strains		
Biological samples		
Chemicals, peptides, and recombinant proteins		
Lysolecithin (L-α-Lysophosphatidylcholine)	Sigma-Aldrich	L4129; CAS: 9008-30-4
Avertin (tribromoethanol)	Sigma-Aldrich	T48402, CAS: 75-80-9
4’,6-diamidino-2-phenylindole, dihydrochloride (DAPI)	Thermo Fisher	62247, CAS: N.A.
ProLong Gold mounting medium	Life Technologies	P36930, CAS: N.A.
Glutaraldehyde	EMS	16000, CAS: 111-30-8
Paraformaldehyde	EMS	15710, CAS: 30525-89-4
Sodium cacodylate	EMS	12300, CAS: 6131-99-3
Epoxy resin EMbed-812	EMS	14120, CAS: N.A.
Fluorescein sodium salt	Sigma-Aldrich	46960, CAS: 518-47-8
Poly-D-lysine	Sigma-Aldrich	P6407, CAS: 27964-99-4

Papain	Worthington	Cat# LS003126, CAS: N.A.
Trypsin	Sigma-Aldrich	Cat# T9935, CAS: N.A.
Dulbecco’s Modified Eagle’s Medium (high glucose)	Thermo Fisher	11960–044, CAS: N.A.
Neurobasal medium	Gibco	Cat# 21103–049, CAS: N.A.
Earle’s balanced salt solution	Sigma-Aldrich	Cat# E7510, CAS: N.A.
Fetal calf serum	GIBCO	Cat# 10437–028, CAS: N.A.
Dulbecco’s PBS (dPBS)	GIBCO	Cat# 14040182, CAS: N.A.
Penicillin/ Streptomycin	Gibco	15140–122, CAS: N.A.
Glutamine	Thermo Fisher	25030–081, CAS: 56-85-9
Sodium pyruvate	Thermo Fisher	11360–070, CAS: 113-24-6
Insulin	Sigma-Aldrich	I6634, CAS: 11061-68-0
N-Acetyl-L-cysteine	Sigma-Aldrich	A8199, CAS: 616-91-1
Trace Elements B	Corning	25022CI, CAS: N.A.
d-Biotin	Sigma-Aldrich	B4639, CAS: 58-85-5
Bovine Serum Albumin	Sigma-Aldrich	A4161, CAS: 9048-46-8
Transferrin	Sigma-Aldrich	T1147, CAS: 11096-37-0
Putrescine	Sigma-Aldrich	P5780, CAS: 333-93-7
Progesterone	Sigma-Aldrich	P8783, CAS: 57-83-0
Sodium selenite	Sigma-Aldrich	S5261, CAS: 10102-18-8
Forskolin	Sigma-Aldrich	F6886, CAS: 66575-29-9
CNTF	Peprotech	450–13, CAS: N.A.
PDGF-AA	Peprotech	100–13A, CAS: N.A.
NT-3	Peprotech	450–03, CAS: 130939-66-1
B-27	Thermo Fisher	17504–044, CAS: 128446-35-5
T3	Sigma-Aldrich	T6397, CAS: 6893-02-3
Phalloidin	Thermo Fisher	A12379, CAS: 17466-45-4
Bolt 4–12% Bis-Tris Plus Gel	Thermo Fisher	NW04120, CAS: N.A.
Nitrocellulose membrane	Thermo Fisher	IB23002, CAS: N.A.
Dexamethasone	Sigma-Aldrich	D4902, CAS: 50-02-2
Aphidicolin	Sigma-Aldrich	178273, CAS: 38966-21-1
Beetle luciferin potassium salt	Promega	E1602, CAS: 115144-35-9
QIAzol Lysis Reagent	Qiagen	79306, CAS: N.A.
BSL1	Vector Laboratories	L1100, CAS: N.A.
Critical commercial assays		
SuperScript™ III First-Strand Synthesis System	Thermo Fisher	18080051, CAS: N.A.
Power Up SYBR Green Master Mix	Applied Biosystems	A25776, CAS: N.A.
NEBNext Ultra II RNA Library Prep	NEB	E7775, CAS: N.A.
Click-iT EdU cell proliferation kit	Life Technologies	C10339, CAS: N.A.
Deposited data		
mRNA-seq, OPCs, Bmal1 WT, ZT0, rep 1	This paper	GSM7667057

mRNA-seq, OPCs, Bmal1 WT, ZT0, rep 2	This paper	GSM7667058
mRNA-seq, OPCs, Bmal1 WT, ZT0, rep 3	This paper	GSM7667059
mRNA-seq, OPCs, Bmal1 WT, ZT0, rep 4	This paper	GSM7667060
mRNA-seq, OPCs, Bmal1 WT, ZT6, rep 1	This paper	GSM7667061
mRNA-seq, OPCs, Bmal1 WT, ZT6, rep 2	This paper	GSM7667062
mRNA-seq, OPCs, Bmal1 WT, ZT6, rep 3	This paper	GSM7667063
mRNA-seq, OPCs, Bmal1 WT, ZT6, rep 4	This paper	GSM7667064
mRNA-seq, OPCs, Bmal1 WT, ZT6, rep 5	This paper	GSM7667065
mRNA-seq, OPCs, Bmal1 WT, ZT12, rep 1	This paper	GSM7667066
mRNA-seq, OPCs, Bmal1 WT, ZT12, rep 2	This paper	GSM7667067
mRNA-seq, OPCs, Bmal1 WT, ZT12, rep 3	This paper	GSM7667068
mRNA-seq, OPCs, Bmal1 WT, ZT12, rep 4	This paper	GSM7667069
mRNA-seq, OPCs, Bmal1 WT, ZT12, rep 5	This paper	GSM7667070
mRNA-seq, OPCs, Bmal1 WT, ZT12, rep 6	This paper	GSM7667071
mRNA-seq, OPCs, Bmal1 WT, ZT18, rep 1	This paper	GSM7667072
mRNA-seq, OPCs, Bmal1 WT, ZT18, rep 2	This paper	GSM7667073
mRNA-seq, OPCs, Bmal1 WT, ZT18, rep 3	This paper	GSM7667074
mRNA-seq, OPCs, Bmal1 WT, ZT18, rep 4	This paper	GSM7667075
mRNA-seq, OPCs, Bmal1 KO, ZT0, rep 1	This paper	GSM7667076
mRNA-seq, OPCs, Bmal1 KO, ZT0, rep 2	This paper	GSM7667077
mRNA-seq, OPCs, Bmal1 KO, ZT0, rep 3	This paper	GSM7667078
mRNA-seq, OPCs, Bmal1 KO, ZT0, rep 4	This paper	GSM7667079
mRNA-seq, OPCs, Bmal1 KO, ZT6, rep 1	This paper	GSM7667080
mRNA-seq, OPCs, Bmal1 KO, ZT6, rep 2	This paper	GSM7667081
mRNA-seq, OPCs, Bmal1 KO, ZT6, rep 3	This paper	GSM7667082
mRNA-seq, OPCs, Bmal1 KO, ZT6, rep 4	This paper	GSM7667083
mRNA-seq, OPCs, Bmal1 KO, ZT6, rep 5	This paper	GSM7667084
mRNA-seq, OPCs, Bmal1 KO, ZT6, rep 6	This paper	GSM7667085
mRNA-seq, OPCs, Bmal1 KO, ZT6, rep 7	This paper	GSM7667086
mRNA-seq, OPCs, Bmal1 KO, ZT12, rep 1	This paper	GSM7667087
mRNA-seq, OPCs, Bmal1 KO, ZT12, rep 2	This paper	GSM7667088
mRNA-seq, OPCs, Bmal1 KO, ZT12, rep 3	This paper	GSM7667089
mRNA-seq, OPCs, Bmal1 KO, ZT12, rep 4	This paper	GSM7667090
mRNA-seq, OPCs, Bmal1 KO, ZT18, rep 1	This paper	GSM7667091
mRNA-seq, OPCs, Bmal1 KO, ZT18, rep 2	This paper	GSM7667092
mRNA-seq, OPCs, Bmal1 KO, ZT18, rep 3	This paper	GSM7667093
mRNA-seq, OPCs, Bmal1 KO, ZT18, rep 4	This paper	GSM7667094
Experimental models: Cell lines		
Experimental models: Organisms/strains		
Mouse: B6;FVB-Ifi208Tg(Cspg4-cre)1Akik/J	The Jackson Laboratory	RRID: IMSR_JAX: 008533

Mouse: B6N.Cg-Tg(Pdgfra-cre/ERT)467Dbe/J	The Jackson Laboratory	RRID: IMSR_JAX: 018280
Mouse: B6.129S4(Cg)-Bmal1^{tm1Weit}/J	The Jackson Laboratory	RRID: IMSR_JAX: 007668
Mouse: B6.129S6-Per2^{tm1Jt}/J	The Jackson Laboratory	RRID: IMSR_JAX: 006852
Oligonucleotides		
Oligonucleotides for genotyping	See Table S5	N.A.
Oligonucleotides for RT-qPCR analysis	See Table S5	N.A.
Recombinant DNA		
Software and algorithms		
ImageJ	NIH	https://imagej.net/Downloads
Incucyte ZOOM	Essen Bioscience	https://www.essenbioscience.com/es/resources/incucyte-zoom-resources-support/software-modules-incucyte-zoom/
VitalView	Mini Mitter	https://www.starrlifesciences.com/resource/vitalview-software-download/
SleepSign	Kissei Comtec Co. Ltd.	https://sleepsign-for-animal.software.informer.com/download/
CatWalk XT 9.0	Noldus Information Technology	https://catwalk-xt.software.informer.com/
Ethovision XT	Noldus Information Technology	https://ethovision-xt.software.informer.com/
ZenBlue	Zeiss	https://www.zeiss.com/microscopy/en_us/products/microscope-software/zen.html
Image Studio Lite	LI-COR	https://www.licor.com/bio/image-studio-lite/
Imaris for Neuroscientists Cell Imaging Software ver. 9.8.	Oxford Instruments	https://imaris.oxinst.com/products/imaris-for-neuroscientists
GraphPad Prism	Dotmatics	https://www.graphpad.com:443/
Hisat2 v2.0.5	N.A.	http://daehwankimlab.github.io/hisat2/
FeatureCounts v1.5.0-p3	N.A.	https://subread.sourceforge.net/featureCounts.html
Profiler R package	N.A.	https://cran.r-project.org/web/packages/profileR/index.html
TwoSampleMR package version 0.5.6 with R version 4.1.3.	N.A.	https://mrcieu.github.io/TwoSampleMR/news/index.html
mRnd	N.A.	https://shiny.cnsgenomics.com/mRnd/
Other		
Telemetry device G2 E-Mitter	Mini Mitter	G2 E-Mitter
Low-torque slip-ring commutator	Biella Engineering	N.A.
Glass amplifier	West Warwick	N.A.
Sleep recording system Vital Recorder	Kissei Comtec Co. Ltd.	N.A.
Confocal microscope Zeiss LSM900	Zeiss	LSM900
Transmission Electron Microscope	Jeol USA	JEOL JEM-1400 TEM
Microplate reader	Molecular Devices	SpectraMax iD3
Peristaltic pump	VWR	70730–062

WesternBright Sirius	Advansta	K-12043-C20
QuantStudio™ 6 Flex Real-Time PCR System	Applied Biosystems	N.A.
Boyden chambers	Corning	CLS3422
NovaSeq 6000 S4 system	Illumina	N.A.